CHAPTER 4

RESULTS AND DISCUSSION

Results and discussion

4.1 Heterocyclic substituted Triazine as corrosion steel for carbon(N-80) steel.

The present work selected the 1,3,5-Triazine (s-triazine) derivatives as corrosion inhibitors based on their structures, biological profile, and nontoxic nature [(Brzozowski, Sączewski, and Gdaniec 2000; Menicagli *et al*. 2004; Afonso, Lourenco, and Rosatella 2006)]. The presence of lone pair of electrons on nitrogen atoms, π-electron on the phenyl ring, is an important structural feature through which they can easily adsorb on the metal surface and bring down corrosion. A few triazine derivatives have been reported as corrosion inhibitors [(Yadav *et al*. 2015; Prajila, Ammal, and Joseph 2018; El-Faham *et al*. 2016; Yoo *et al*. 2015; Shukla, Singh, and Quraishi 2012)]. A perusal of the literature shows that there are no reports using corrosion inhibitors for N80 steel in 15% HCl. Synthesis of selected molecules has been carried out in higher yield, shorter reaction time, and milder conditions using the ultra-sonication method [(Cintas and Luche 1999; J.-T. Li *et al*. 2003))]. All three synthesized triazines (TZs) were characterized by ^{1}H NMR, ^{13}C NMR, and FTIR. Their corrosion inhibition behavior on mild steel in hydrochloric acid has been investigated using gravimetric studies, electrochemical measurements, and surface analysis. The molecular structure and abbreviations of the synthesized substituted triazine derivative are given in Figure 4.1.

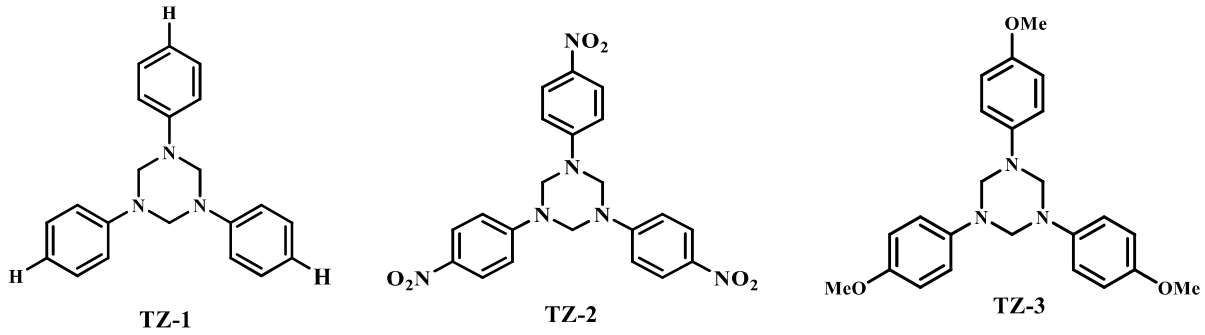

Figure 4.1 Structure of inhibitors: TZ-1, TZ-2, and TZ-3.

4.1.1 Weight loss measurements

4.1.1.1. Effect of inhibitor concentration.

The observation of Figure 4.2 reveals that inhibition efficiency and corrosion rate are increasing and decreasing, respectively, with increasing TZs concentration from 200 to 800 mg/L. This is due to the adsorption of TZs molecules over the metal surface, thereby reducing the metal sample exposed to the acidic solution [(Nadi *et al*. 2019)]. Indeed, the upsurge in inhibition efficiency as the TZs concentration increased from 200 to 800 mg/L can be caused by enhanced surface coverage at higher concentrations through the adsorption of TZs molecules onto the metal surface.

The order of inhibition efficiency is as follows: TZ-3 (92%) > TZ-1 (85%) > TZ-2(78%). The corrosion protection ability of TZ-3 is highest due to the presence of the electron-donating OCH_3 group. At the same time, TZ-2 has the lowest because of the electron-withdrawing nitro (NO_2) group. The further increase in TZs concentration does not significantly affect inhibition efficiency and corrosion rate values. Thus, 800 mg/L was selected as the optimum concentration.

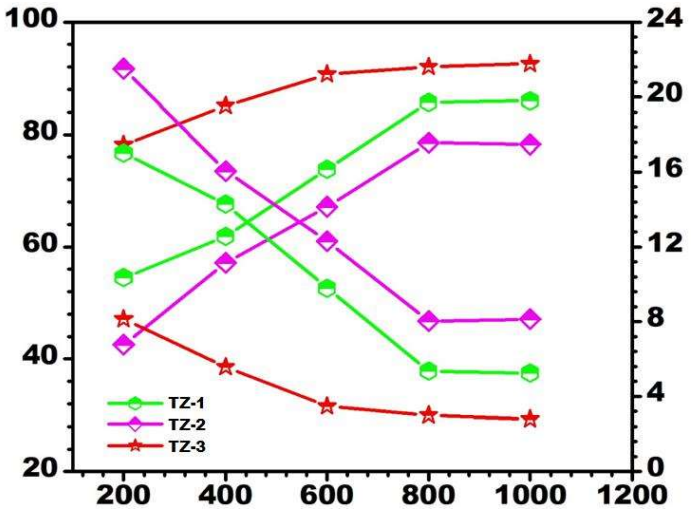

Figure 4.2 Variation of inhibition efficiency (η%) and corrosion rate (ν_{corr}).

4.1.1.2 *Adsorption isotherm*

The study of adsorption isotherm becomes necessary to investigate the interaction ability of the TZs molecules with the N80 steel surface. The surface coverage values (θ) are used to calculate the suitable adsorption isotherm at 35^0C temperature in 15% HCl. The preferable isotherm can be justified based on either R^2 or slope values. Various isotherms like Temkin Flory-Huggins, Frumkin, Freundlich, and Langmuir have been fitted using θ values with inhibitor concentration. In the present investigation, the best fit is obtained with the Langmuir adsorption isotherm with the R^2 and slope values close to 1 (Table 4.1). Mathematically Langmuir adsorption isotherm model is given as follows [(Singh *et al.* 2019)]:

Table 4.1 Calculated values of various isotherms for N80 steel in 15% HCl at the optimum concentration (800 mg/L) of TZs.

Isotherm	Inhibitor	R2	Slope
Temkin	TZ-3	0.986	0.239
	TZ-1	0.913	0.484
	TZ-2	0.981	0.579
Frumkin	TZ-3	0.992	7.763
	TZ-1	0.930	8.357
	TZ-2	0.960	8.592
Flory-Huggins	TZ-3	0.941	1.137
	TZ-1	0.740	0.738
	TZ-2	0.898	0.771
Freundlich	TZ-3	0.999	0.877
	TZ-1	0.987	0.690
	TZ-2	0.998	0.564
Langmuir	TZ-3	0.998	1.016
	TZ-1	0.962	0.932

$$\frac{C_{inh}}{\theta} = \frac{1}{K_{ads}} + C_{inh} \qquad (4.1)$$

C_{inh} is the concentration (M) of TZs, and K_{ads} is the adsorption-desorption equilibrium constant. Pictorially the Langmuir isotherm displayed in Figure 4.3, that is, a relationship between C_{inh} and (C_{inh}/θ).

The K_{ads} values were estimated from the intercept of the Langmuir plots. The obtained K_{ads} values were used for the calculation of ΔG^0_{ads} (standard free energy change of adsorption) applying equation 3.13: Where R is the universal gas constant, T is the absolute temperature, and 55.55 is a constant associated with the concentration of water molecules. The values of K_{ads} and ΔG^0_{ads} are tabulated in Table 4.2. In the current investigation, The

K_{ads} values are large, suggesting the strong adsorption of TZs molecules over the N80 steel surface. However, the ΔG^0_{ads} values are in the range of physical and chemical adsorption, revealing a combined mechanism of the adsorption process [(Singh *et al*. 2019)]. In addition to this, the negative values of ΔG^0_{ads} reveal the spontaneous nature of the adsorption process [(Manimegalai and Manjula 2015)].

Table 4.2 Thermodynamic parameters for the adsorption of TZs on N80 steel in 15% HCl.

Solution	K_{ads} (M^{-1})	ΔG^0_{ads} (kJ mol^{-1})
TZ-3	8030	−33.31
TZ-1	2010	−29.77
TZ-2	1447	−28.92

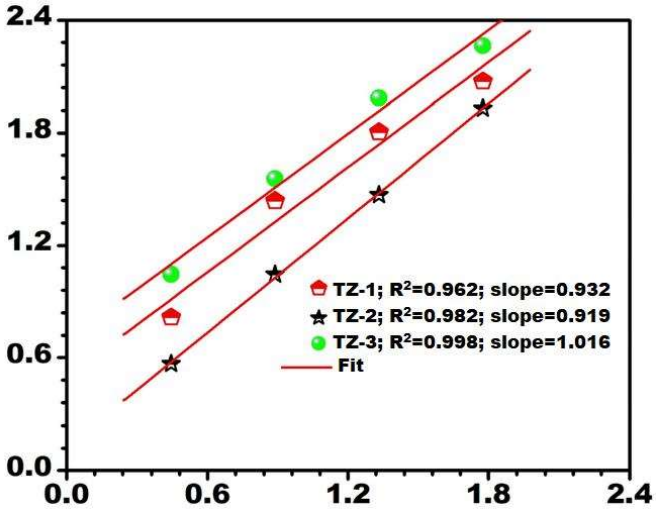

Figure 4.3. Langmuir isotherm plot for the adsorption of TZs on N80 steel surface in 15% HCl.

4.1.2 Electrochemical studies.

4.1.2.1 Electrochemical Impedance Spectroscopy.

EIS uses to study the kinetics involved in the electrochemical process of corrosion inhibition reactions taking place on the N80 steel surface in 15% HCl solution at 35^0C. Figures 4.4A-C and 4.5A-C present the fitted Nyquist and Bode plots at different concentrations (200-800 mg/ L) of the TZs and blank (TZs free), respectively.

Nyquist plots consist of a single semicircle that suggests that the dissolution of N80 steel in 15% HCl is under the charge transfer control process. In the Nyquist plots, the size of the semicircle is larger in the presence of TZs as compared to TZs-free solution. Also, with increase in the concentration of TZs, the size of the semicircle increases, which signifies that the metal surface becomes more corrosion-resistant. Observation suggests that a protective TZs film has been formed over the metal surface due to the adsorption of the TZs molecules [Srivastava *et al*. (2018)]. The electrochemical impedance parameters were calculated by fitting the equivalent circuit (Figure 4.5a). The fitted Nyquist and Bode plots can demonstrate the fitting accuracy of the equivalent circuit. The impedance elements residing in the equivalent circuit consist of the constant phase element (CPE), which is parallel to the charge transfer resistance (R_{ct}). They are in series with the solution resistance (R_s) [(Vakili Azghandi *et al*. 2012)].

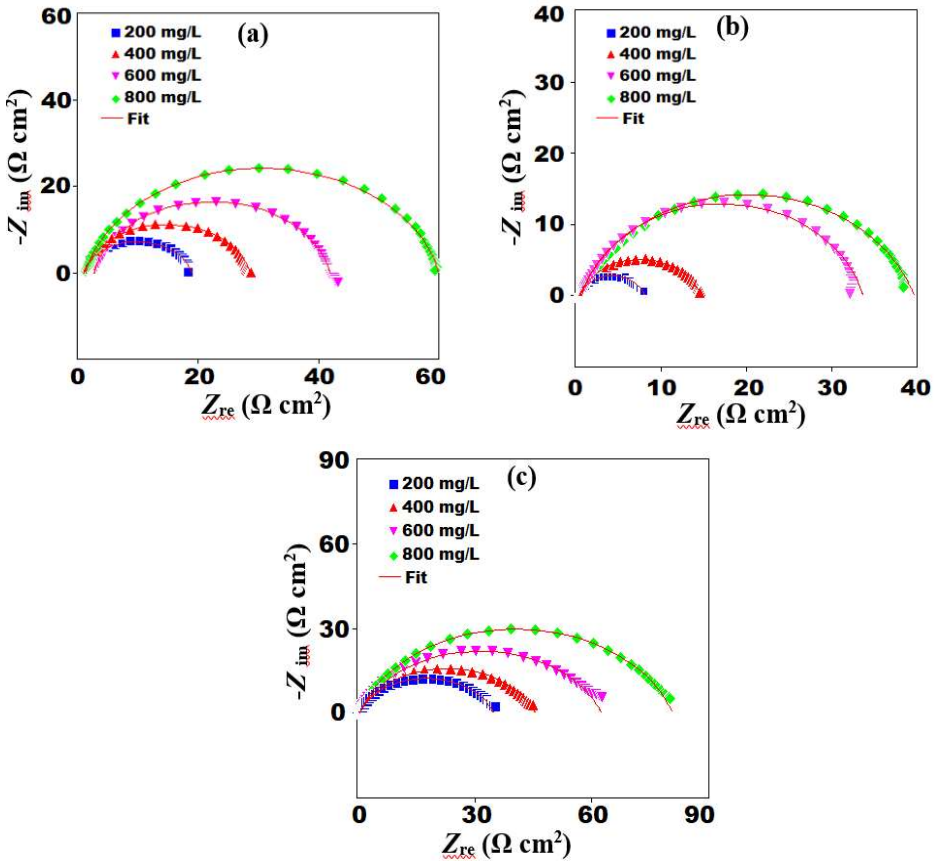

Figure 4.4 Nyquist plot for mild steel in 1 mol L^{-1} HCl without and with different concentrations of TZs. (a)TZ-1 (b) TZ-2 (c)TZ-3.

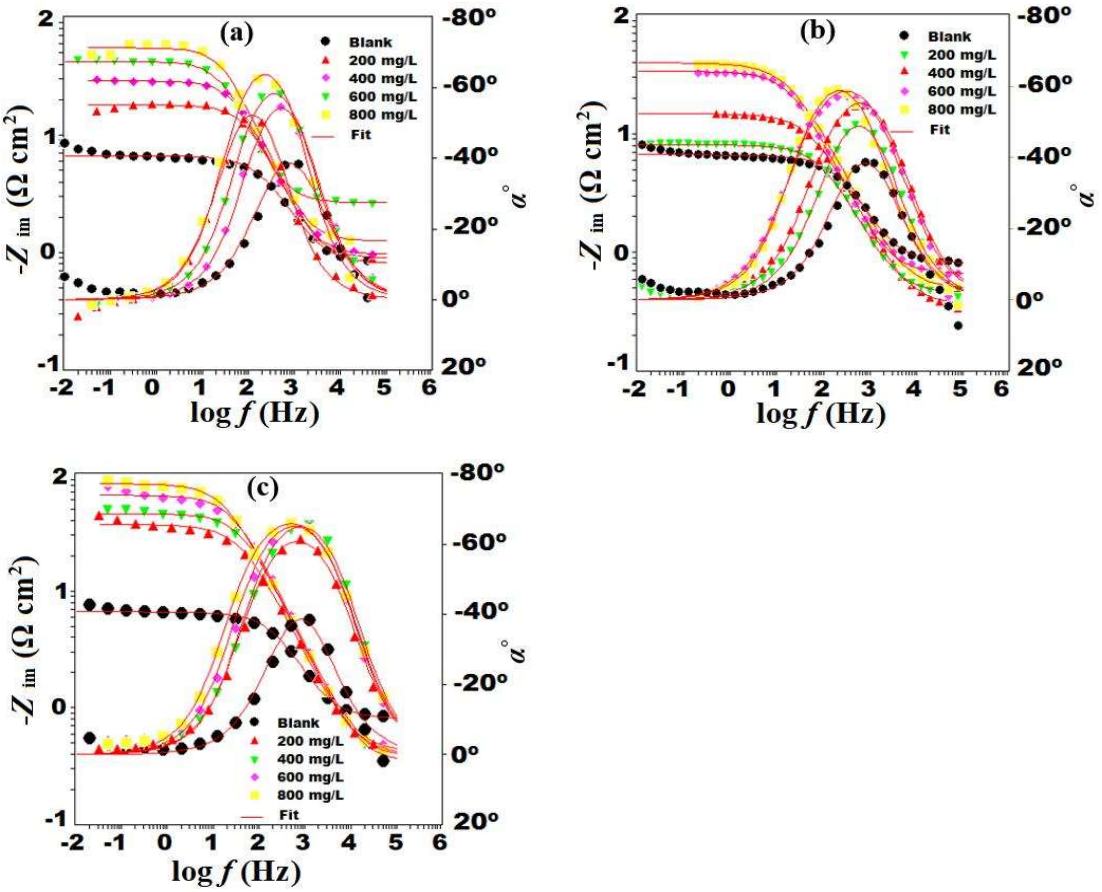

Figure 4.5 Bode (f vs |Z|) and phase angle (f vs αo) plot for N80 steel in 15% HCl without and with different concentrations of TZs.

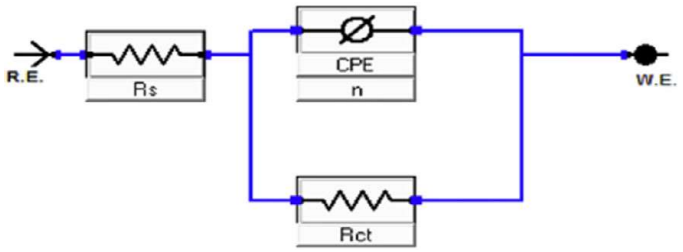

Figure 4.5 (a) Equivalent circuit

The Nyquist plots do not have perfect semicircles, but they are depressed under the real axis. This is because the N80 steel is not homogenous and has a rough surface. So, to calculate an accurate result, double layer capacity (C_{dl}) was replaced by the CPE in the equivalent circuit (Figure 4.5 a). The relation of CPE with the impedance follows equation 3.6:

Where ω is the angular frequency, Y_o is the admittance, a constant for the CPE proportionality coefficient, j is the imaginary number, and n, is the measure of surface inhomogeneity [Mizuno *et al*. (2012)]. In the inhibitor-free (TZs) solution, the n value is less as compared to the addition of increasing concentration of the TZs from 200 to 800 mg/ L. This is quite common that the N80 steel surface is inhomogeneous and rough without the inhibitor addition.

Table 4.3 Electrochemical impedance parameters of N80 steel in 15% HCl at different concentrations of TZs at 308 K.

C_{inh} (mg/L)	R_s (Ω)	R_{ct} (Ω cm^2)	Y_0 (μF/cm^2)	n	C_{dl} (μF/cm^2)	η (%)	α^0
Blank	0.82	5.404	406	0.755	72.1		−39.09
TZ-3							
200	0.408	34.0	250	0.765	69.3	84.1	−65.94
400	0.342	44.8	180	0.801	63.5	87.9	−65.78
600	0.419	61.6	110	0.852	53.51	91.2	−65.49
800	0.377	80.223	45	0.892	27.0	93.2	−61.54
TZ-1							
200	1.013	16.7	289	0.76	70.0	67.8	−62.89
400	0.429	27.9	223	0.778	66.3	80.6	−59.17
600	2.649	36.4	150	0.788	54.3	85.1	−54.64
800	1.258	57.5	101	0.811	40.6	90.6	−52.53
TZ-2							
200	0.45	7.1	327	0.752	71.5	24.8	−49.15
400	0.364	15.1	250	0.763	68.6	64.2	−54.82
600	0.669	32.4	192	0.780	59.8	83.3	−57.17
800	0.489	38.7	147	0.806	55.7	86.0	−59.09

While the increasing concentration of TZs, the N80 steel surface becomes more homogeneous because of the adsorption of the TZs molecules. The Double-layer capacitance (C_{dl}) can be calculated using Expression [3.6]:

The inhibition efficiency (ηEIS%) was calculated using equation 3.7:

Where R and $R_{(inh)}$ are the charge transfer resistance without and with the studied inhibitor, respectively. Impedance results of EIS and Bode obtained after fitting the equivalent circuit are tabulated in Table 4.3. A closer examination of Table 4.3 data reveals that the increasing concentration of the TZs causes an increase in the R_{ct} values and a decrease in

the C_{dl} values. The above statement can be explained by the fact that with increasing TZs concentration, more adsorption of the inhibitor molecules occurs at the metal surface, which causes an increase in its corrosion resistance property, and finally, R_{ct} values increase. The decreasing values of the C_{dl} with increasing concentration of the TZs are due to the lowering of the dielectric constant residing in the metal solution interface and/or increment in the thickness of the double layer, which is achieved by substituting the pre-adsorbed water molecules from the N80 steel surface with the TZs molecules. Thus, results obtained from the EIS measurement reveal that the inhibition action of the TZs molecules at the N80 steel/HCl interface is via adsorption.

In the Bode phase angle plots (Figure 4.5A-C and Table 4.3) at the intermediate frequency, the phase angle values (α) increase with the TZs concentration. This reveals that the addition of inhibitor molecules causes to increase in the homogeneity of the metal surface due to the adsorption. The assessment of Table 4.3 suggests that the performance of the TZ-3 is better than TZ-1 and TZ-2. This is because TZ-3 has an electron-donating $-OCH_3$ group attached to the phenyl ring. Therefore, the order of the inhibition efficiency is as follows: TZ-3 (93.2%) > TZ-1 (90.6%) > TZ-2 (86.0%). Thus, the presence of different substituents in the inhibitor molecules plays an important role in the adsorption and corrosion inhibition performance.

4.1.2.2 Potentiodynamic polarization study.

The PDP curves of N80 steel without and with different concentrations of TZs in 15% HCl at 35^0C are represented graphically in Figure 4.6A-C.

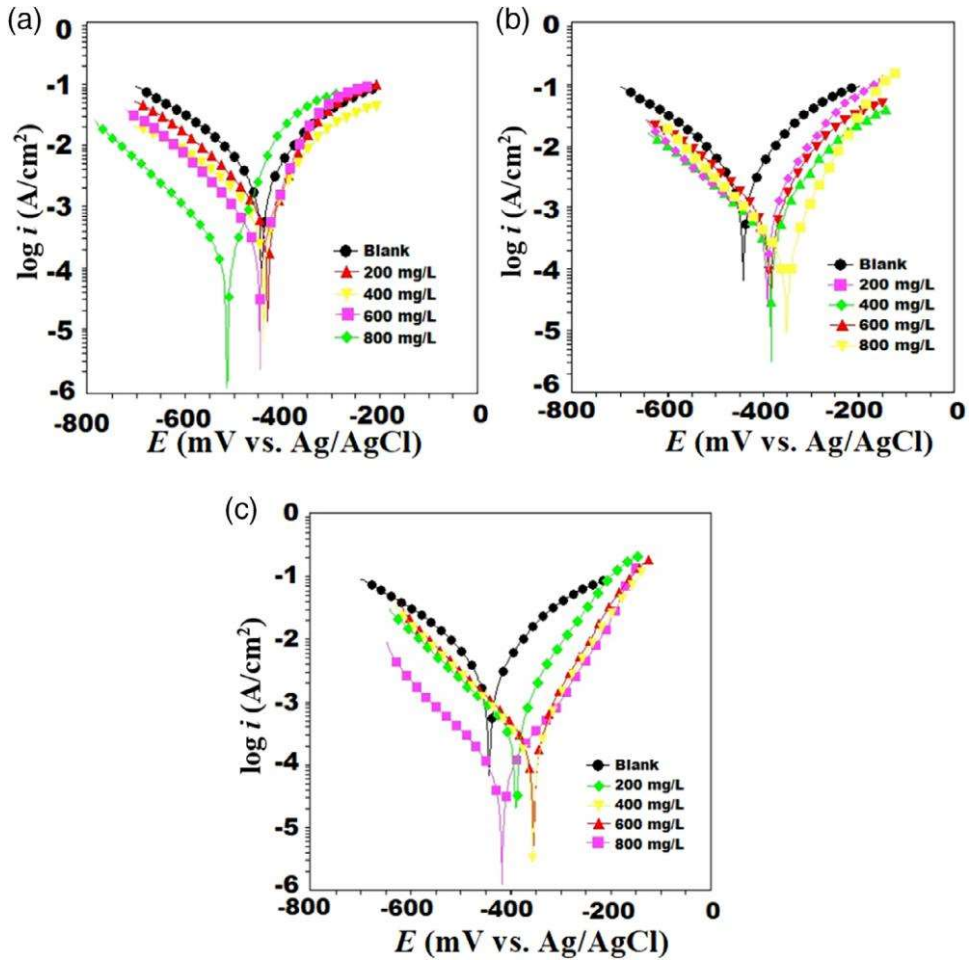

Figure 4.6 Potentiodynamic polarization curves for N80 in the absence and presence of different concentrations of TZs 35^{0}C. (a) TZ-1, (b) TZ-2, (c) TZ-3.

The observation of the figures suggests a remarkable influence of the TZs addition over the PDP curves, which means both the anodic and cathodic Tafel lines shifted towards the lower current density, and this shift is maximum at the highest concentration (800 mg/L). This suggests that TZs molecules are efficient in retarding the corrosion of N80 steel by suppressing both the cathodic hydrogen evolution reaction and the anodic metal dissolution

reaction [(Abd El-Lateef and Alnajjar 2020)]. Some important polarization parameters such as corrosion current density (i_{corr}), corrosion potential (E_{corr}), cathodic (βc), and anodic (βa) Tafel slopes were tabulated in Table 4.4. The given equation did the calculation of inhibition efficiency (ηPDP%):

$$\eta_{PDP\%} = \frac{i_{corr} - i_{corr(inh)}}{i_{corr}} x100 \qquad (4.2)$$

I_{corr} and i_{corr} (inh) are the current densities without and with the inhibitor, respectively.

In the present analysis, TZs act as mixed-type inhibitors [(Abd El-Lateef and Alnajjar 2020, 20)] The change in the values of Tafel slopes, that is, βc and βa as per Table 4.4, are decidedly less without and with increasing concentration of TZs, which suggests that the addition of TZs into the corrosive media did not change the mechanism of corrosion reactions. Thus, the inhibition action of TZs molecules over the N80 steel surface is governed by the formation of an adsorbed and stable protective film [(Achary et al. 2008) Achary *et al*. (2008)].

The analysis of Table 4.4 reveals that the values of the inhibition efficiency increased from 67 to 93% (TZ-3), 55 to 87% (TZ-1), and 39% to 85% (TZ-2) with increasing the TZs concentration. While the values of corrosion current density (i_{corr}) decrease from 1630 μAcm^{-2} (TZs free) to 108 μAcm^{-2} (TZ-3), 196 μAcm−2 (TZ-1), and 230 μAcm^{-2} (TZ-2), respectively, at 800 mg/L of TZs concentration. The increase in inhibition efficiency and decrease in corrosion current density is due to the adsorption of TZs molecules onto the N80 steel/HCl interface [(Achary *et al*. 2008)]. The order of inhibition efficacy is as TZ- 3

> TZ-1 > TZ-2. The inhibition of the efficiency of TZ-3 is better than TZ-1 and TZ-2 due to the presence of an electron-donating OCH_3 group. The obtained result of PDP is inconsistent with the EIS result.

Table 4.4 Electrochemical polarization parameters in the absence and presence of different concentrations of triazine derivative at 308 K.

Inhibitor (mg/L)	E_{corr} (mV/SCE)	i_{corr} (μA/cm2)	βa (mV/dec)	-βc (mV/dec)	η (%)
Blank	−443	1630	86	101	
TZ-3					
200	−389	532	71	196	67.3
400	−355	271	70	144	83.3
600	−356	206	71	130	87.3
800	−418	108	123	150	93.3
TZ-1					
200	−430	722	64	115	55.7
400	−439	68	82	135	57.9
600	−447	299	54	102	81.6
800	−514	196	63	126	87.9
TZ-2					
200	−392	988	82	152	39.3
400	−385	803	85	158	50.7
600	−384	587	95	157	64.0
800	−351	230	64	134	85.8

4.1.3 Surface studies.

4.1.3.1 UV-visible spectroscopy.

The interaction of metal and inhibitor was studied using UV-visible spectroscopic analysis. The UV-visible absorption spectra obtained from 15% M HCl solution containing 800 mg/L of TZ-1, TZ-2, and TZ-3 before and after 24 h of N80 steel immersion at 308 K are

shown in Figure 4.7. The absorption spectra of TZs before immersion of N80 steel consist of the following bands; 203.3, 264.4 nm (TZ-1), 202.3, 261.5 nm (TZ-2), and 223.4, 272.9 nm (TZ- 3). However, after immersion of N80 steel, the electronic absorption spectra give some shifting, and the bands are as follows; 209.9, 238.6 nm (TZ-1), 205.2, 254.8 nm (TZ-2), and 221.5, 268.3 nm (TZ-3), and the occurrence of these bands are due to the π-π* and n-π* transitions. It is important to note that the addition of N80 steel causes a shift in the bands and an increase in the absorbance. These findings are indicative of the interaction of the TZs molecules with the N80 steel surface [(Obot, Obi-Egbedi, and Eseola 2011)].

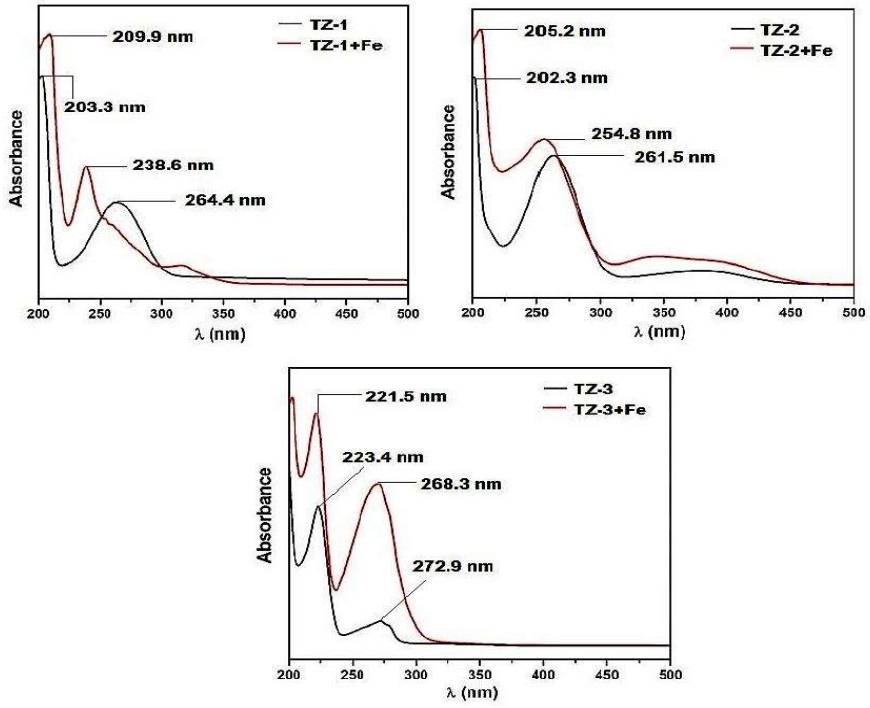

Figure 4.7 UV–visible spectra. (A) TZ-1, (B) TZ-2, (C) TZ-3

4.1.3.2 FTIR spectral analysis.

The FTIR characteristics of the TZs film formed on the N80 steel surface are presented in Figure 4.8. In the case of the pure TZs, characteristic peaks have been discussed earlier in section 3.1. In the adsorbed TZs, broadband around 3300 cm^{-1} is attributed to the O-H stretching, which suggests the formation of FeOOH. However, the aromatic C-H stretching, C-N, and C=C bands intensities in the region between 1600 and 600 cm^{-1} become weaker after the adsorption of TZs over the N80 steel surface (Figure 4.8. This result confirms the involvement of these centers in the adsorption phenomenon, which further leads to the formation of TZs film onto the N80 steel surface [(de Souza and Spinelli 2009; Vengatesh, Karthik, and Sundaravadivelu 2017; X. Li, Deng, and Fu 2012)].

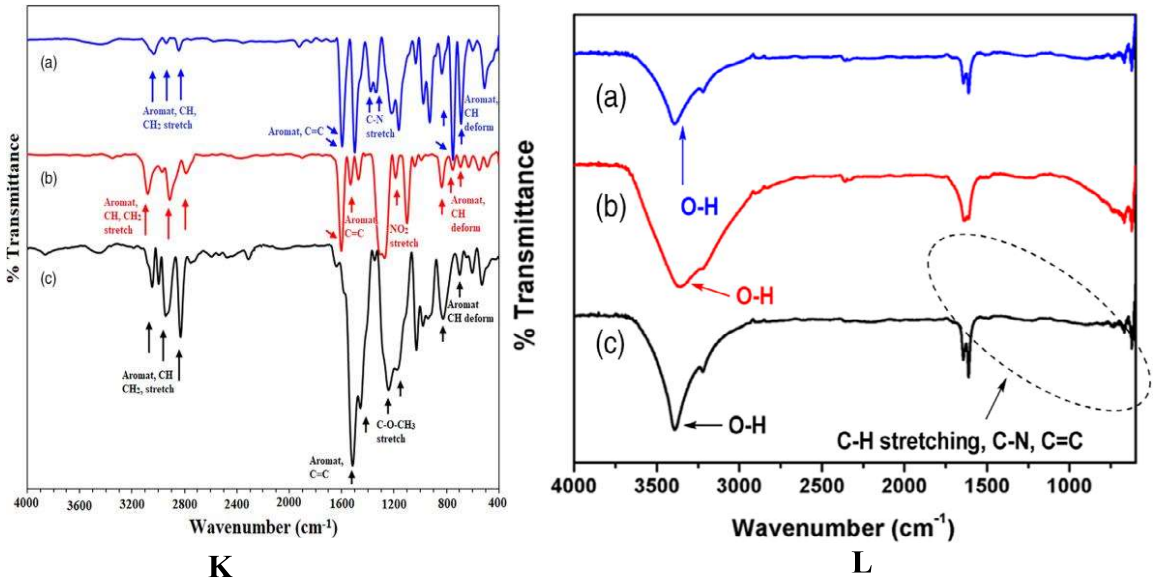

Figure 4.8 FTIR spectra of the inhibitors (**K**). (**a**) TZ-1(**b**) TZ-2, (**c**) TZ-3, FTIR spectra of adsorbed inhibitor molecules on the N80 steel surface **(L)**. (**a**) TZ-1, (**b**) TZ-2, (**c**) TZ-3.

4.1.3.3 Atomic force microscopy (AFM) characterization.

The analysis of surface morphology using the AFM technique can be represented by 3D-dimensional images (Figure 4.9A-D) and their corresponding height profile diagram (Figure 4.9 E-H). The 3D image of the N80 steel without adding TZs reveals that the metal surface was damaged severely because of the corrosive attack of the 15% HCl (Figure 4.9A). The corresponding height profile diagram (Figure 4.9E) consists of the peaks and valleys around 300 nm height, and the calculated average roughness (R_a) is 127 nm. However, the addition of TZs in the corrosive medium reduces the destructive attack of the aggressive medium, which is observed in the 3D images (Figure 4.9 B-D). In addition to this, the height profile diagrams of TZs further confirmed that the surface becomes smooth because their corresponding height curves (Figure 4.9 F-H) are 60 nm (TZ-1), 100 nm (TZ-2), and 10 nm (TZ-3). The calculated Ra values from the height profile diagrams were reduced to 26 nm (TZ-1), 40 nm (TZ-2), and 6 nm (TZ-1) as compared to TZs free 127 nm. [Aslam *et al*. (2018)] The reduction of the average roughness values (Ra) suggests that TZs molecules have adsorbed on the N80 steel surface and reduced the corrosion process. [(Singh *et al.* 2019)] The AFM results further confirm the order of inhibition efficiency obtained from the weight loss and electrochemical measurement studies.

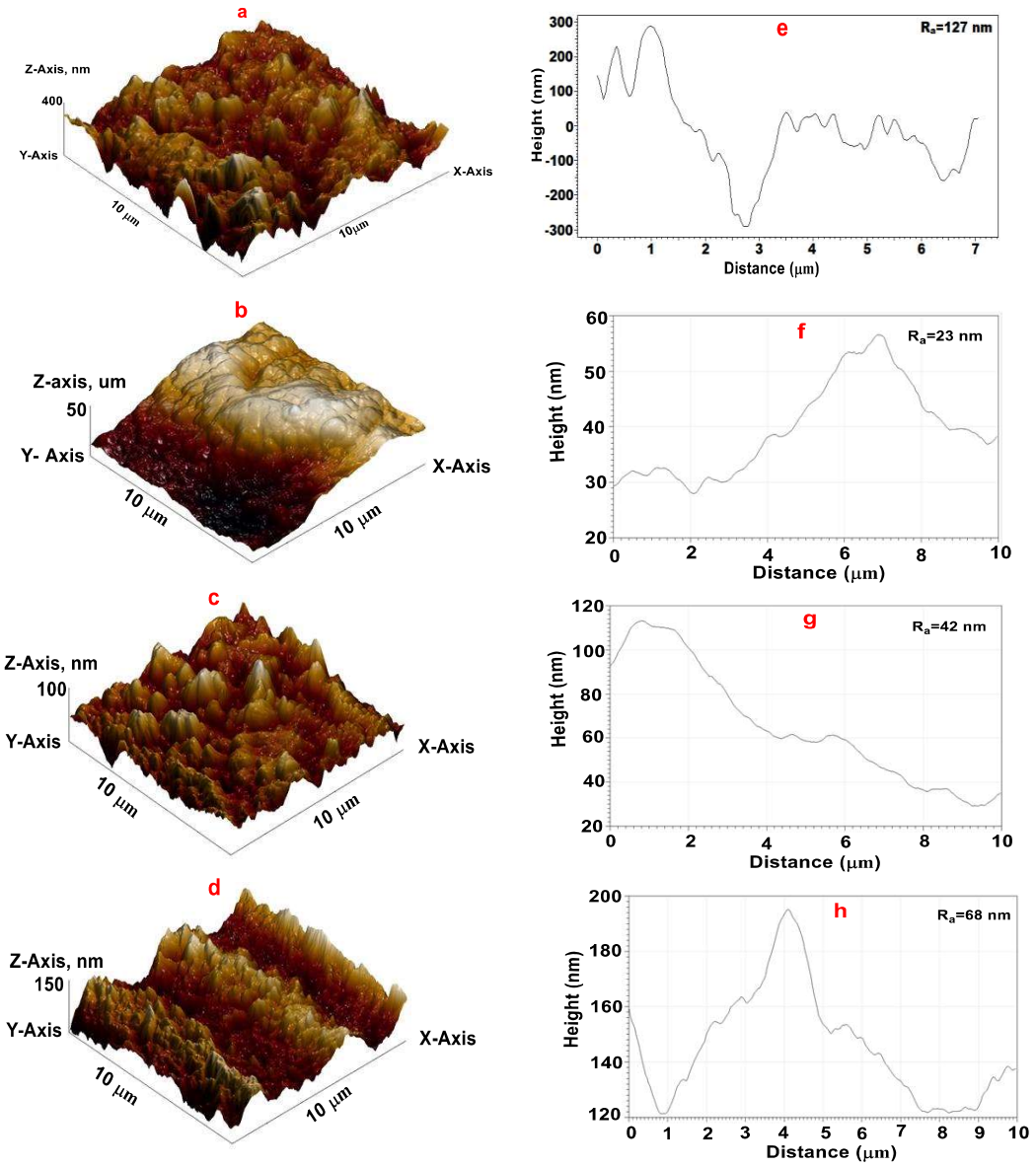

Figure 4.9 Three dimension AFM images and corresponding height profile diagram of N80 steel: **(a, e)** without TZs, **(b, f)** with TZ- 2, **(c, g)** TZ-1 **(d, h)** with TZ-3.

4.1.4 Mechanism of inhibition

The PDP results indicate that the mixed character of TZs adsorption and ΔG^0_{ads} reflects both the chemical and physical (mixed) nature of inhibitor adsorption. The iron dissolving mechanism in HCl at the anodic site is as follows:

$$Fe + Cl \rightleftarrows (FeCl)^-_{ads} \quad (4.3)$$

$$(FeCl^-)_{ads} \rightleftarrows (FeCl)_{ads} + e^- \quad (4.4)$$

$$(FeCl)_{ads} \rightleftarrows (FeCl^+) + + e^- \quad (4.5)$$

$$(FeCl^+) \rightleftarrows Fe^{+2} + Cl^- \quad (4.6)$$

The protonated inhibitor molecules ($TZsH^+$) adsorbed at the anodic site as per the below reaction:

$$(FeCl^-)_{ads} + TZsH^+ \rightarrow (FeCl^-TZsH^+)_{ads} \quad (4.7)$$

Thus, the protonated inhibitor ($TZsH^+$) molecules can be electrostatically (physically) adsorbed on the N80 steel surface, preventing the anodic corrosion process [(Umoren *et al.* 2019)].

In the same way, the mechanism of the cathodic reaction is as follows:

$$Fe + H^+ \rightarrow (FeH^+)_{ads} \quad (4.8)$$

$$(FeH^+)_{ads} + e^- \rightarrow (FeH)_{ads} \quad (4.9)$$

$$(FeH)_{ads} + H^+ + e^- \rightarrow Fe + H_2 \quad (4.10)$$

The protonated inhibitors ($TZsH^+$) molecules can also adsorb at cathodic sites, compete with H^+ for electrons, and reduce H_2 evolution. Inhibitor adsorption is also accomplished

through a chemical process that begins with the displacement of adsorbed water molecules from the N80 steel/solution contact. The TZs molecules have lone pairs of electrons provided to the vacant iron orbitals by the heteroatoms and -electrons donated to the phenyl rings, establishing coordinate bonds (chemical adsorption [(Solomon *et al*. 2018)]. Both experimentally observed results are supported by the described inhibitory mechanism.

4.1.5 Conclusions.

The ultrasound approach made it simple to manufacture three triazine derivatives. The triazines produced demonstrated promising corrosion inhibition of N80 steel in 15% HCl. These inhibitors have the potential to be utilized in the oil and gas industries as acidizing corrosion inhibitors. Excellent agreement was obtained in the values of the corrosion inhibition efficiency obtained from weight loss and electrochemical analyses. The corrosion inhibition efficiency was found to increase with the rise in temperature suggesting chemical adsorption of the inhibitors on the steel surface. The adsorption of the inhibitors obeys Langmuir isotherm, and the value of ΔG^0_{ads} demonstrates a spontaneous adsorption process. The EIS results showed an increase in charge transfer resistance and a decrease in double-layer capacitance, indicating the creation of an inhibitor coating on the steel surface. The PDP tests revealed that triazines function as a mixed-type inhibitor. The AFM experiments confirm a considerable reduction in the roughness of the steel surface following the addition of the inhibitors to the corrosive solution. Surface roughness was reduced in the presence of triazines, according to AFM measurements. The chemical interaction of the inhibitors with the metal surface was confirmed by FTIR and UV-vis investigations.

4.2 Chromeno naphthyridines based heterocyclic compounds as novel acidizing corrosion inhibitors.

Acidization is an important and effective technique for increasing oil wells production. The basic principle in acidization involves injecting hydrochloric acid (HCl) in the range of 15-28% into an oil well through the production tubing that is commonly made of N80 steel [(Shafiq and Mahmud 2017; Crowe, Masmonteil, and Thomas 1992)]. This process makes the N80 steel corrode. To minimize the acid's corrosive nature, inhibited acid solutions are added.

Among heterocycles, chromeno naphthyridines have received special attention because they exhibit a wide range of biological activities such as antibacterial, antimycobacterial, antiallergic, antitumor, anti-aggressive, anti-inflammatory, antihypertensive, antimalarial, which make them biologically inspired molecules [(Gohil, Patel, and Patel 2016)]. However, these compounds have adverse effects on living beings and the environment due to their toxic and non-degradable nature [(Neemla *et al*. 1989; Frenier, Growcock, and Lopp 1988)]. Therefore, corrosion scientists have focused their attention on exploring environmentally benign corrosion inhibitors, e.g. plant extracts [(Hussin *et al*. 2016; Alaneme, Olusegun, and Adelowo 2016)]. Some synthetic organic compounds [(E. Ituen, Asuquo, and Essien 2017; E. B. Ituen and Asuquo 2019; L. Zhang *et al*. 2015)] are being used as corrosion inhibitors. However, they are not effective as corrosion inhibitors in a strongly acidic environment. In the present work, three chromeno naphthyridine derivatives

have been synthesized using one pot multicomponent reaction (MCR) and evaluated as corrosion inhibitors on N80 steel. MCR is a green approach to the synthesis of organic compounds. In this approach, several components are taken in one reaction flask. The benefits of MCRs include high yield, high atom economy, a simple workup process, and mild reaction conditions. In the present work, synthesis has been carried out using green solvents (water), reusable catalysts (silica gel), and less toxic chemicals that fulfill the guidelines of the green chemistry concept [Razvan *et al*. (2014)]. The selection criteria of these compounds as potential corrosion inhibitor depends on the following reasons: (1) From a structural point of view, these molecules possesses three nitrogen and one oxygen atom, and π-electrons that will act as regions for adsorption, (2) They are planar molecules. (3) Presence of substituents like $–NH_2$, -CN, -OH enhance their solubility as well as inhibitive performance. (4) Biological activities associated such as anticonvulsant activity, anti-human cytomegalovirus (HCMV) inhibitors, and antitumor activity make them environmentally benign corrosion inhibitors [(Madaan et al. 2015)]. (5) The predicted LD_{50} values are 340 mg/kg (CN-1), 1500 mg/kg (CN-2) and 800 mg/kg (CN-3) [(Banerjee *et al*. 2018)]. Our group has a strong background in the development of environmentally benign acidizing corrosion inhibitors [(Singh et al. 2020; 2018)]. The performance of these compounds as acidizing corrosion inhibitors is reported for the very first time.

The corrosion inhibition potential of synthesized compounds namely 5-amino-9-hydroxy-2-(4-vinyl phenyl)-1,11b-dihydrochromeno[4,3,2-de][1,6]naphthyridine-4-carbonitrile (CN-1),5-amino-9-nhydroxy-2-(4-methoxyphenyl)-1,11b-dihydrochromeno[4,3,2-de][1,6]

naphthyridine-4-carbonitrile (CN-2), 5-amino-9-hydroxy-2-phenyl-1,11b-dihydrochromeno[4,3,2-de][1,6]naphthyridine-4-carbonitrile (CN-3) have been tested over N80 steel in acidizing environment (15% HCl). The methods used for analysis involve weight loss, electrochemical impedance (EIS), and potentiodynamic polarization (PDP). Morphological investigation of N80 steel surface was examined by FTIR, AFM, and UV–vis. Finally, the results were further validated with DFT calculations and Molecular dynamic simulation (MDS).

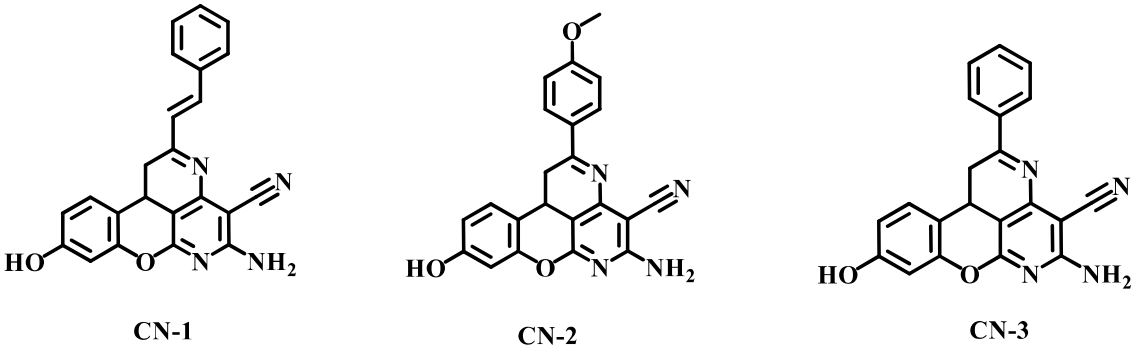

Figure 4.10 Structure of inhibitors: CN-1, CN-2, and CN-3.

4.2.1 Weight loss measurements

4.2.1.1 Effect of concentration.

Figure 4.11, represents the variation in inhibition efficiency and corrosion rate with concentration at 35°C temperature. The observation of Figure 4.11, reveals that increasing the concentration of CNs leads to a decrease and increase in corrosion rate and inhibition efficiency values, respectively. This kind of phenomenon is because of CNs molecules' adsorption over the metal surface, which makes inhibitor molecules cover more surface of the steel. The selection of 300 mg/L the as optimum

concentration is due to the insignificant changes in the values of corrosion rate/inhibition efficiency after increasing the concentration beyond 300 mg/L. This suggests selecting 300 mg/L as the optimum concentration.

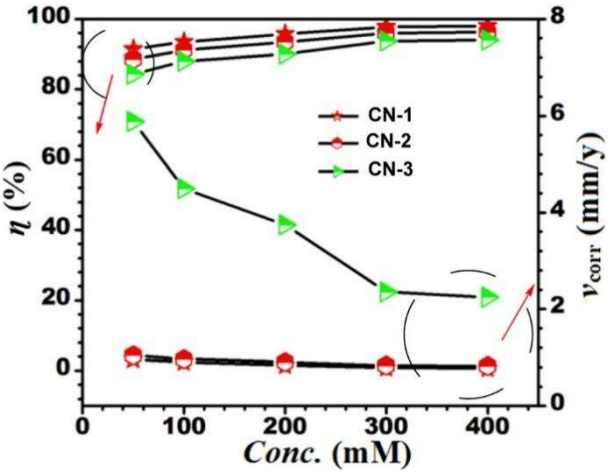

Figure 4.11 Variation of inhibition efficiency (η%) and corrosion rate (νcorr).

4.2.1.2 Adsorption studies.

In the present paper, after fitting various kinds of isotherms, only Langmuir isotherm, i.e., C/θ vs. C represents the best fitting, displaying the formation of monolayer of inhibitor film. This kind of selection is based on the closeness of R^2 and slope values to 1 Figure following equation 4.1.

Where concentration, surface coverage, and equilibrium adsorption constants are represented by θ, C_{inh}, and K_{ads}. The calculated values of equilibrium adsorption constant, i.e., K_{ads} using the straight-line of intercepts. It is reasonable to say that the adsorption of CNs is strong due to the high values of K_{ads} [(Mohammadi and Rahsepar 2019)]. The standard free energy ($\Delta G°_{ads}$) is calculated using the values of the equilibrium adsorption

constant (K_{ads}) as per the given equation 3.14: Where gas constant and temperature are represented by R and T, respectively, the concentration of water is 55.5 mol L^{-1}. The calculated values of K_{ads} are 95,238 M^{-1} (CN-1), 80,000 M^{-1} (CN-2), 74,074 M^{-1} (CN-3) and $\Delta G°_{ads}$ − 39.65 M^{-1} (CN-1), −39.20 M^{-1} (CN-2), −39.00M^{-1} (CN-3). The spontaneous nature of CNs adsorption is reflected by negative values of $\Delta G°_{ads}$ [(Badiea and Mohana 2009)]. However, the magnitude of $\Delta G°_{ads}$ reflects the chemical as well as physical (mixed) nature of adsorption processes [(H. H. Zhang and Chen 2019)].

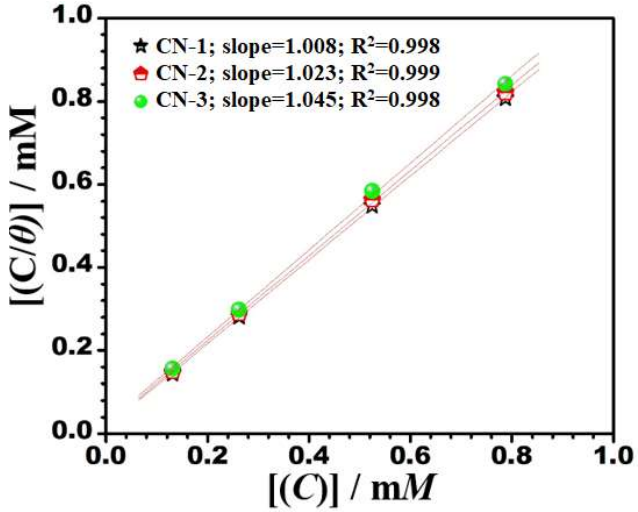

Figure 4.12: Langmuir isotherm plot for the adsorption of CNs on N80 steel surface in 15% HCl.

4.2.2 Electrochemical studies.

4.2.2.1 Electrochemical impedance spectroscopy.

The fitted Nyquist plots represent the N80 steel corrosion in the absence and presence of CNs in 15% HCl and are shown in Figure 4.13a–c. The analysis of the Figure shows that the impedance character changed after adding a different concentration of the CNs as

compared to the blank, in other words, the semicircular arc of Nyquist plots increases with increasing CNs concentration, which suggests that the charge transfer controlled corrosion process [(Tan and Kassim 2011)]. It is noteworthy that the center of the Nyquist plot is under the real axis, which shows the non-perfect nature of the semicircle or depressed semi-circle. This kind of appearance of the Nyquist plot is due to the frequency dispersion that is associated with the metal surface roughness, inhibitor adsorption, porous layer formation, etc. [(Okafor and Zheng 2009)]. The figures represent two kinds of Nyquist plots, one which only consists of an only the capacitive loop and the other one which contains both capacitive loops as well as a small inductive loop. The occurrence of the capacitive loop represents the charge transfer reaction, while inductive attributes the surface coverage by the intermediates such as Cl^- ads and H^+ ads) [(Deng and Li 2012)]. Due to the presence of two kinds of Nyquist curves, two different kinds of equivalent circuits are used (Figure 4.13d, e). To model, the depressed semi-circle perfectly constant phase element (CPE) has been used in the equivalent circuit [(Tan and Kassim 2011)].

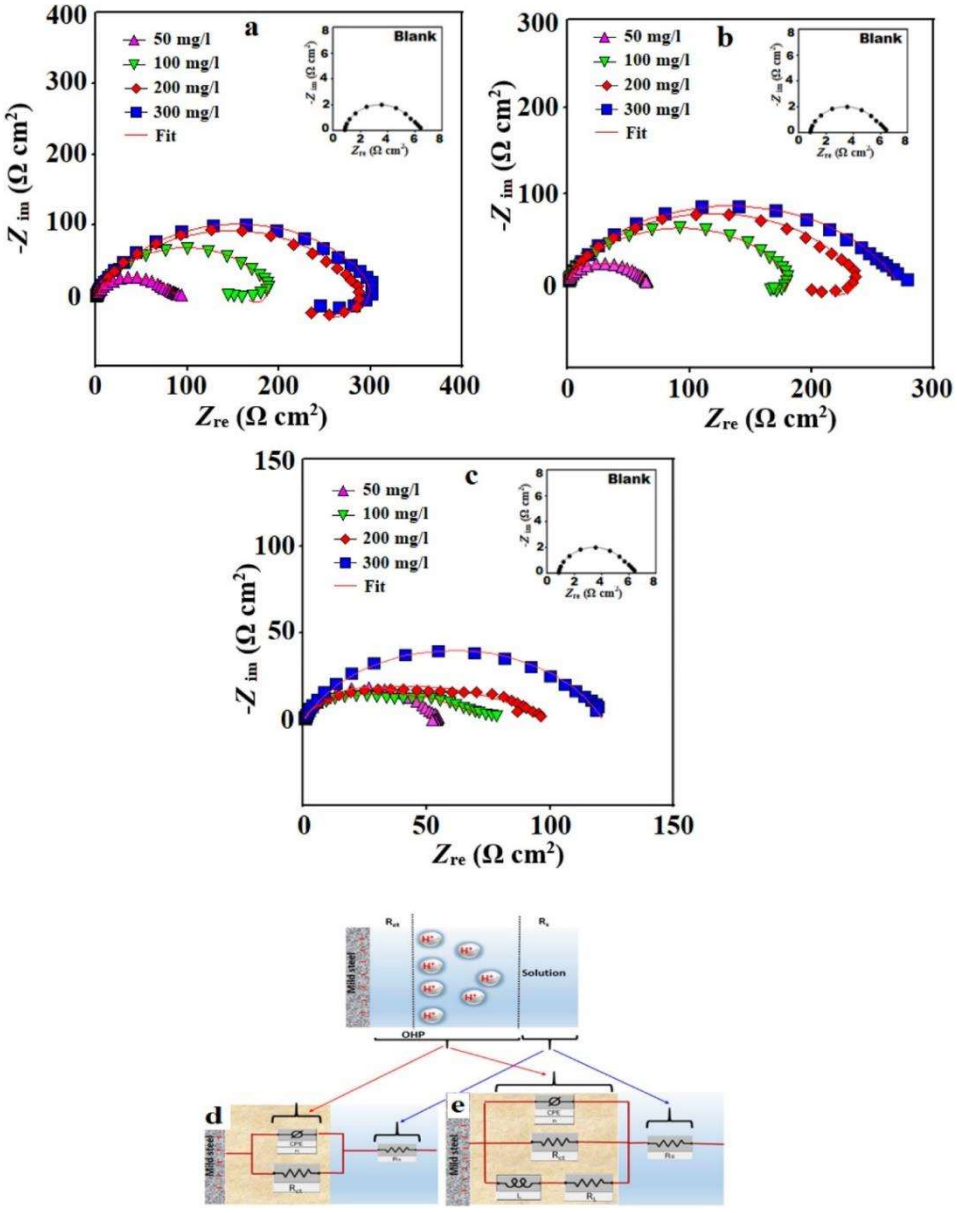
a
50 mg/l
100 mg/l
200 mg/l
300 mg/l
Fit
Blank
-Z im (Ω cm2)
Zre (Ω cm2)
b
50 mg/l
100 mg/l
200 mg/l
300 mg/l
Fit
Blank
-Z im (Ω cm2)
Zre (Ω cm2)
c
50 mg/l
100 mg/l
200 mg/l
300 mg/l
Fit
Blank
-Z im (Ω cm2)
Zre (Ω cm2)

Mild steel
Solution
OHP
d
e
Mild steel
Mild steel

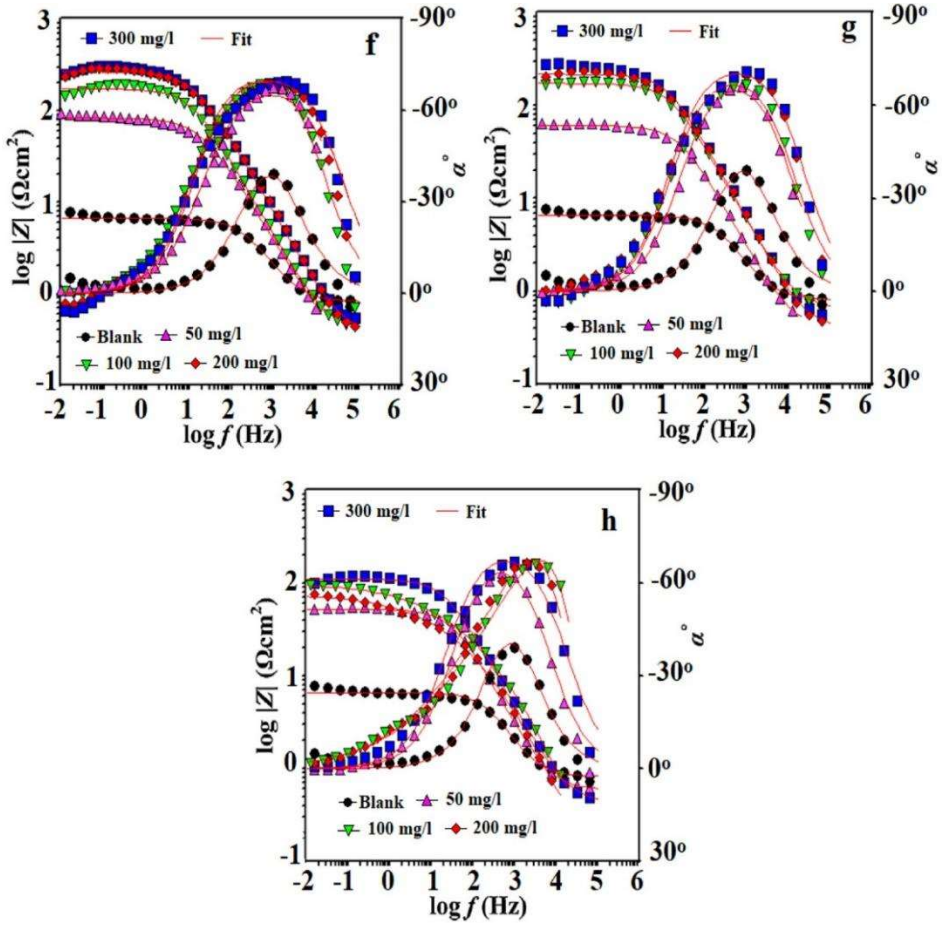

Fig. 4.13. Fitted **Nyquist** plot for N80 steel in 15%HCl without and with different concentrations of CNs at 35 °C (**a**) CN-1 (**b**) CN-2 (**c**) CN-3. **d**,**e**: Equivalent circuit used. **Bode** (f vs |Z|) and phase angle (f vs α_o) plots for N80 steel in 15% HCl without and with different concentrations of CNs 35°C (**f**) CN-1 (**g**) CN-2 (**h**) CN-3.

The essential components present in the equivalent circuit are R_s, R_{ct}, R_L, L, and CPE, representing the resistance of solution, charge transfer resistance, inductive resistance, inductance, and constant phase elements, respectively.

The CPE admittance (Y_{CPE}) and impedance (ZCPE) are calculated using equations 3.5. Where Y_o represents the amplitude comparable to capacitance, j with the magnitude of the root of −1 represents the imaginary number, ω is the angular frequency ($\omega=2\pi\ \upsilon_{max}$), and n represents the roughness and heterogeneity of N80 steel. In the present paper, the calculation of double-layer capacitance (C_{dl}) and inhibition efficiency (η%) values was done using the values of Y_o and n: equation 3.6 shows.

Table 4.5, represents the impedance parameters. Scrutiny of Table 4.5 suggests that R_{ct} values of the inhibited solution are more as compared to the uninhibited one. It is interesting to note that the R_{ct} and η% values are increasing with increasing CNs concentration, which is due to the formation of molecular films of CNs over the interface of N80 steel/solution [Bustamante *et al*. (2009)]. In addition to this, the reduction in the values of Y_o with increasing concentration of CNs suggests that the inhibitor molecules cause the displacement of the water molecules and occupy the vacant sites [(Anzar *et al*. 2018)]. The decrement of the N80 steel surface heterogeneity with the addition of CNs can be visualized by increased values of "n" as compared to the uninhibited solution. This further suggests molecular adsorption of CNs onto N80 steel surface [(Boucherit *et al*. 2018)].

Table 4.5. Electrochemical impedance parameters of N80 steel in 15% HCl at different concentrations of CNs at 35 °C.

Cinh (mg/L)	R_s (Ω)	R_{ct} (Ω cm^2)	Y_0 (μF/cm^2)	n	C_{dl} (μF/cm^2)	L	RL	η (%)	α^0
Blank	0.82	5.404	406	0.755	72.1	--	−39.09		
CN-1									
50	0.225	82.64	167	0.796	65.6			93.4	−70.9
100	0.41	193.6	106	0.825	53.3	4707	991	97.2	−69.3
200	0.354	290.8	85	0.858	49.9	15000	1090	98.1	−68.7
300	0.453	310.3	53	0.897	35.87	15620	1454	98.3	−67.2
CN-2									
50	0.4	63.58	180	0.781	67.1	--	--	91.5	−69.3
100	0.649	182.1	133	0.811	60.5	17720	1347	97	−68.8
200	0.405	238	102	0.833	52.9	18270	1455	97.7	−66.4
300	0.464	267.1	75	0.872	45	--	--	97.9	−64.7
CN-2									
50	0.691	53.7	220	0.767	69	--	--	89	−66.9
100	0.149	72.3	157	0.798	65.9	--	--	92.5	−66.2
200	0.2	93.05	120	0.812	57.6	--	--	94.1	−65.18
300	0.432	122.7	96	0.847	54.2	--	--	95.5	−63.14

As per the table, the incrementing CNs concentration leads to a decrease in the values of Cdl. This is because of either double layer thickness increment or pre-adsorbed water molecules replacement by the CN-1, CN-2, and CN-3 [Ozcan *et al*. (2008)]. However, the rise in R_{ct} is more in CN-1 than in CN-2 and CN-3. This is due to the presence of double bond conjugation in CN-1. Although the performance of CN-2 is better, CN-3 is due to the electron-donating methoxy substituent in the molecular framework of CN-2.

The Bode diagrams are depicted in Figure 4.13f–h. In this, the phase angle plots at intermediate frequency in the presence of CNs represent the increasing values of phase

angle with increasing concentration and these values reached to −70° (CN-1). However, this value is −42.3° for blank (Table 4.5) [(Yadav, Quraishi, and Maiti 2012)]. This suggests that CNs molecules have been adsorbed onto the metal surface, reducing the surface roughness.

4.2.2.2 Potentiodynamic polarization.

The Potentiodynamic polarization curves of corrosion of N80 steel in the absence and presence of CNs in 15% HCl are depicted in Figure 4.14 a–c. The important polarization parameters are given in Table 3. The inhibition efficiency (η%) evaluation was done as per the equation 3.8:

Where i_{corr} and $i_{corr(i)}$ are the density of corrosion current in the absence and presence of CNs, respectively; the visual inspection of the Figure suggests that dissolution of metal at anodic sites and the evolution of hydrogen at cathodic sites have both been affected by the addition of CNs into the corrosive environment. In addition, the introduction of CNs causes to decrease in the current density of both the cathodic and anodic reactions. Analysis of the table suggests the lowering values of the current density of corrosion with increasing CNs concentration. The shifts in the E_{corr} values in the presence of CNs are not significant towards anodic sites respective to the blank. Thus, CNs represent the diverse nature of inhibition action. The increasing concertation of CNs does not alter the values of the cathodic Tafel slope (βc) and anodic Tafel slope (βa) very much (Table 4.6) [Li *et al.* (2009)]. Additionally, the increase in the concentration of CNs causes to increase in the inhibition efficiency values and attain 97% (CN-1), 95.2% (CN-2), and 93.2% (CN-3) at an

optimum concentration (300 mg/L). However, CN-1 has better inhibition protection capability than CN-2 and CN-3. This is due to the presence of double bond conjugation in CN-1.

Table.4.6 Potentiodynamic polarization parameters of N80 steel in 15% HCl at different concentrations of CNs at 35 °C.

Inhibitor conc. (mg/L)	E_{corr} (mV/SCE)	i_{corr} ($\mu A/cm^2$)	β_a (mV/dec)	$-\beta_c$ (mV/dec)	η (%)
Blank	-443	1630	86	101	-
CN-1					
50	−428	229	73	160	85.9
100	−431	135	62	356	91.7
200	−425	88	65	201.2	94.5
300	−403	48	52	188	97
CN-2					
50	−424	333	86	119	79.5
100	-431	240	86	149	85.2
200	-413	186	71	282	88.2
300	-430	77	57	181	95.2
CN-3					
50	-400	449	96	232	72.4
100	-405	344	81	152	78.8
200	-434	243	110	144	85
300	-408	110	59	297	93.2

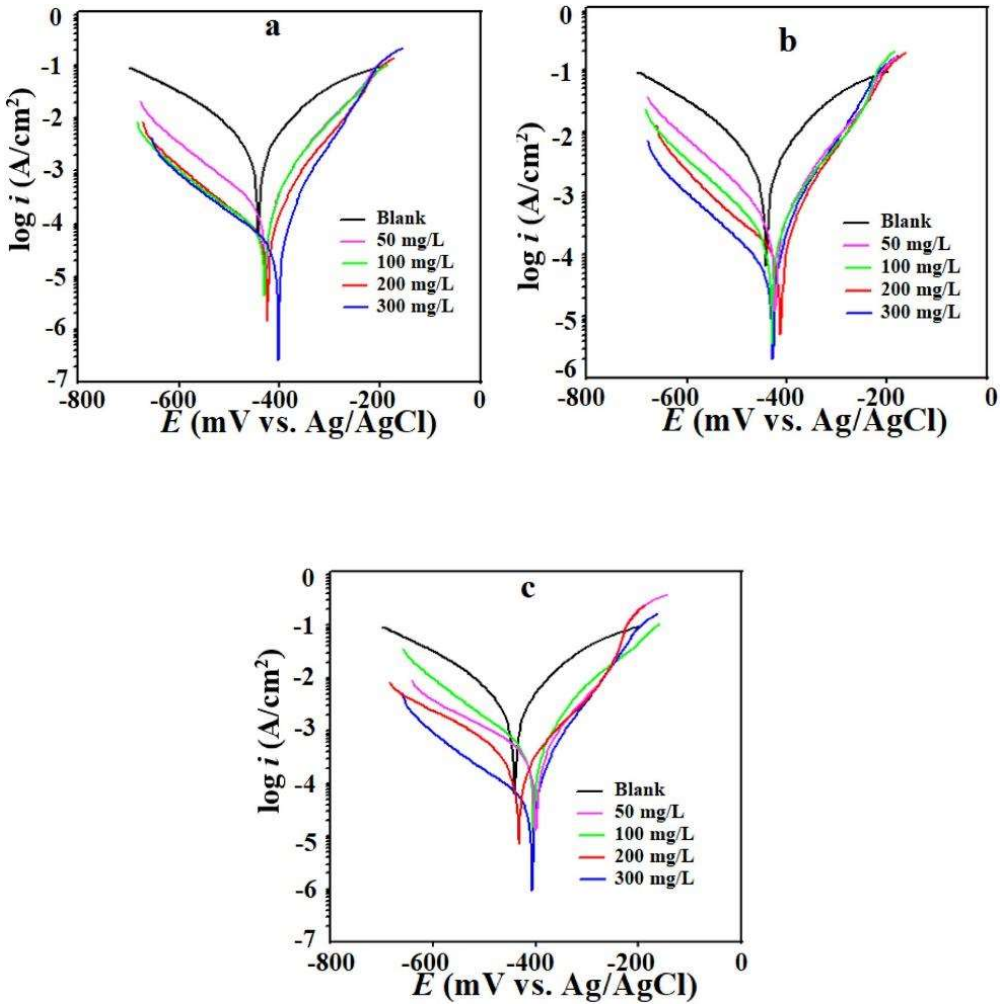

Figure 4.14. Potentiodynamic Polarization curves for N80 steel in the absence and presence of different concentrations of CNs in 15% HCl at 35 °C (a) CN-1 (b) CN-2 (c) CN-3.

4.2.3 Surface studies.

4.2.3.1 Atomic force microscopy (AFM).

Figure 4.15a–h represents the metal surface's 3D and height/distance graphs. The 3D image without adding CNs molecules represents the rough and severely corroded metal surface (Figure 4.15a), and the result of the height profile diagram corresponds to the peaks and valleys value at around 300 nm with an average roughness (R_a) of 127 nm (Figure 4.15e). However, the destructive nature of 15% HCl was reduced after the addition of CNs, which was observed from 3D images (Figure 4.15 2b–d). Additionally, height profile diagrams and average roughness (Ra) (Figure 4.15f–h) values have reduced to 50 nm/23 nm (CN-1), 100 nm/42 nm (CN-2), and 150 nm/68 nm (CN-3) further confirm the smoothness of the metal surface. In the presence of CNs, the decrease in the average roughness (R_a) compared to blank suggests that CNs molecules have adsorbed on the N80 steel surface and act as a barrier between the N80 steel surface and corrosive medium.

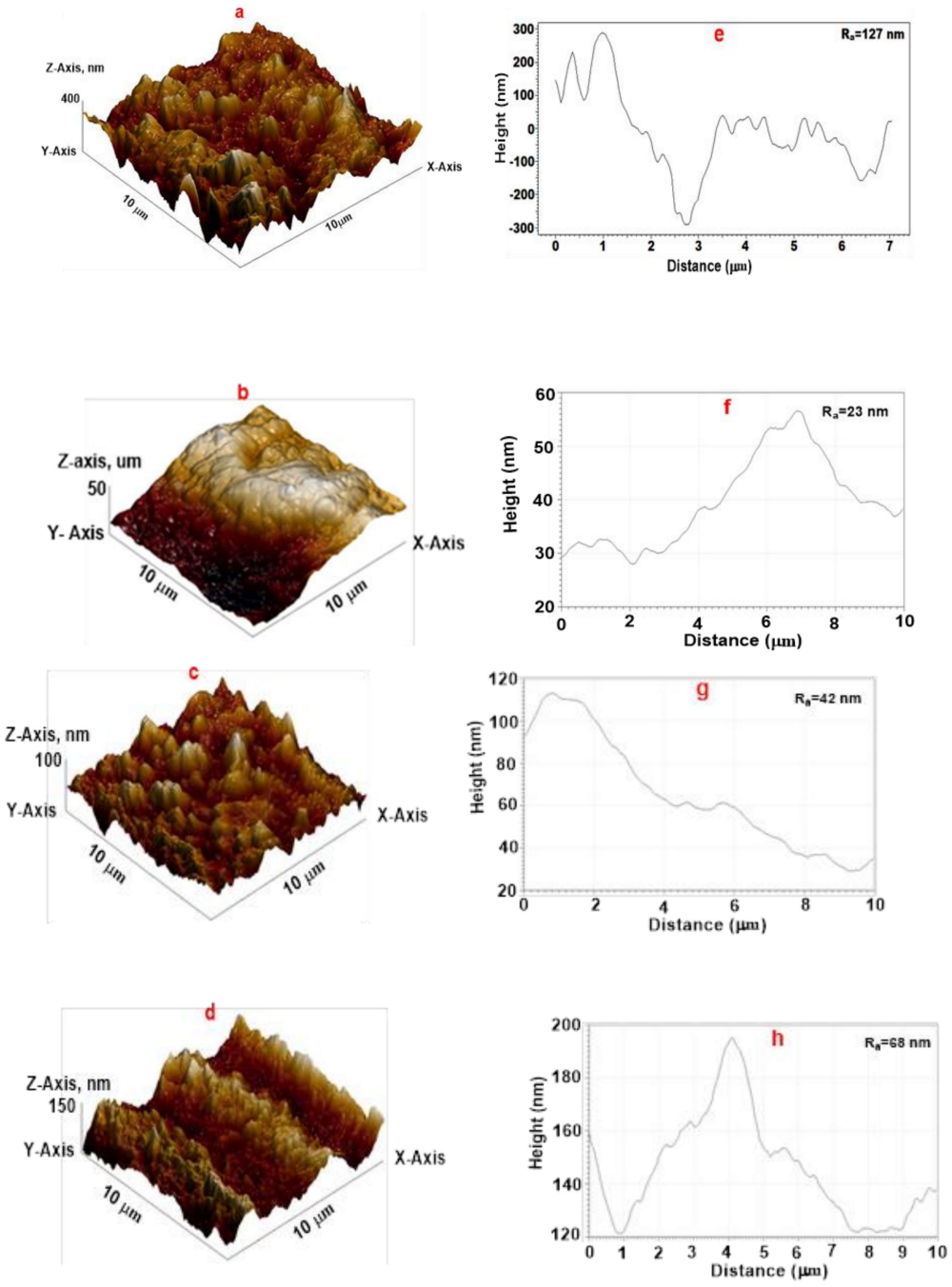

Figure 4.15: Three dimension AFM images and corresponding height profile diagram of N80 steel: **(a, e)** without CNs, **(b, f)** with CN-1 **(c, g)** CN-2 **(d, h)** with CN-3.

4.2.3.2 Fourier-transform infrared spectroscopy (FTIR).

Some significant characteristic peaks of pure CNs have been discussed in section 2.1. In the case of adsorbed CNs, at 3300 cm^{-1}, broadband has appeared, representing the O–H to stretching and corresponding to the formation of FeOOH. However, the bands related to N–H stretching, aromatic, C–H stretching, CN stretching, and C=C almost disappear from the adsorbed spectra (Figure 4.16). This disappearance of the above bands suggests that these regions actively participate in the adsorption process and lead to the formation of CNs molecular film over the N80 steel surface [(de Souza and Spinelli 2009)].

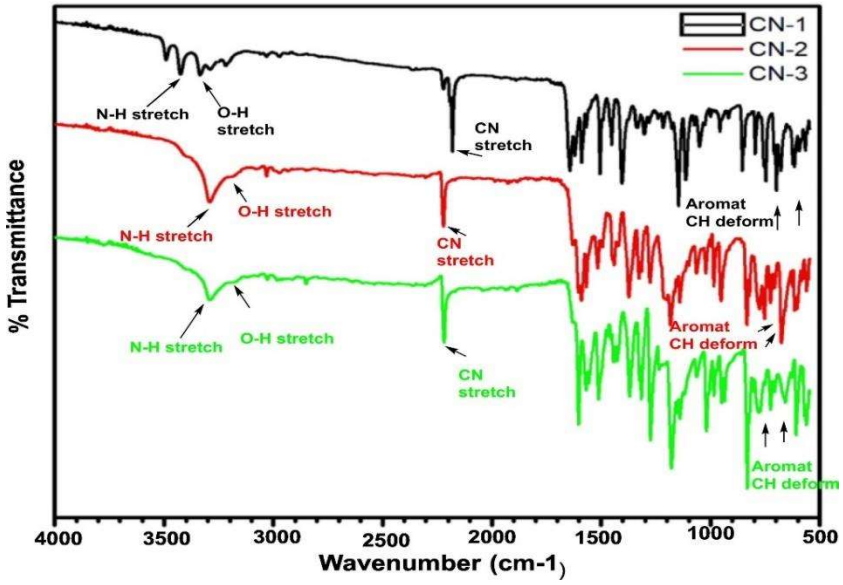

Figure. 4.16: FTIR spectra of adsorbed CNs molecules on the N80 steel surface.

4.2.3.3 Ultraviolet-visible spectroscopy (UV–vis).

The UV–vis spectra of three inhibitors, i.e. CN-1, CN-2, and CN-3, are, depicted in Figure 4.17. The spectra of the pure inhibitor have the following bands; 228.1 nm, 279.7, 306.3 nm (CN-1), 246.5 nm, 271.3 nm, 349.9 nm (CN-2), and 223.3 nm,

308.3 nm, 451.4 nm (CN-3). After the immersion of N80 steel shifting of some bands occurs in CN-1 and CN- 2 but no such change is observed in CN-3. The shifted bands of CN-1 and CN-2 are as follows; 227.2 nm, 306.3 nm (CN-1), 27.1 nm, 277.5 nm, and 308.6 nm (CN-2). These bands correspond to the π–π*, and n–π* transitions. Besides this, a new peak appeared in CN-2 is may be due to the presence of the OCH_3 group that possibly undergoes interaction with the metal. However, no such functional groups are present in CN-1 and CN-3 that could interact and produce new peaks. The change in the absorbance values indicates the complex formation between the inhibitor molecules and the metal surface in the solution. This experimental construction provides evidence forming of a complex between Fe^{2+} and CNs molecules and confirms the inhibition of N80 steel from corrosion [(Obot, Obi-Egbedi, and Eseola 2011)].

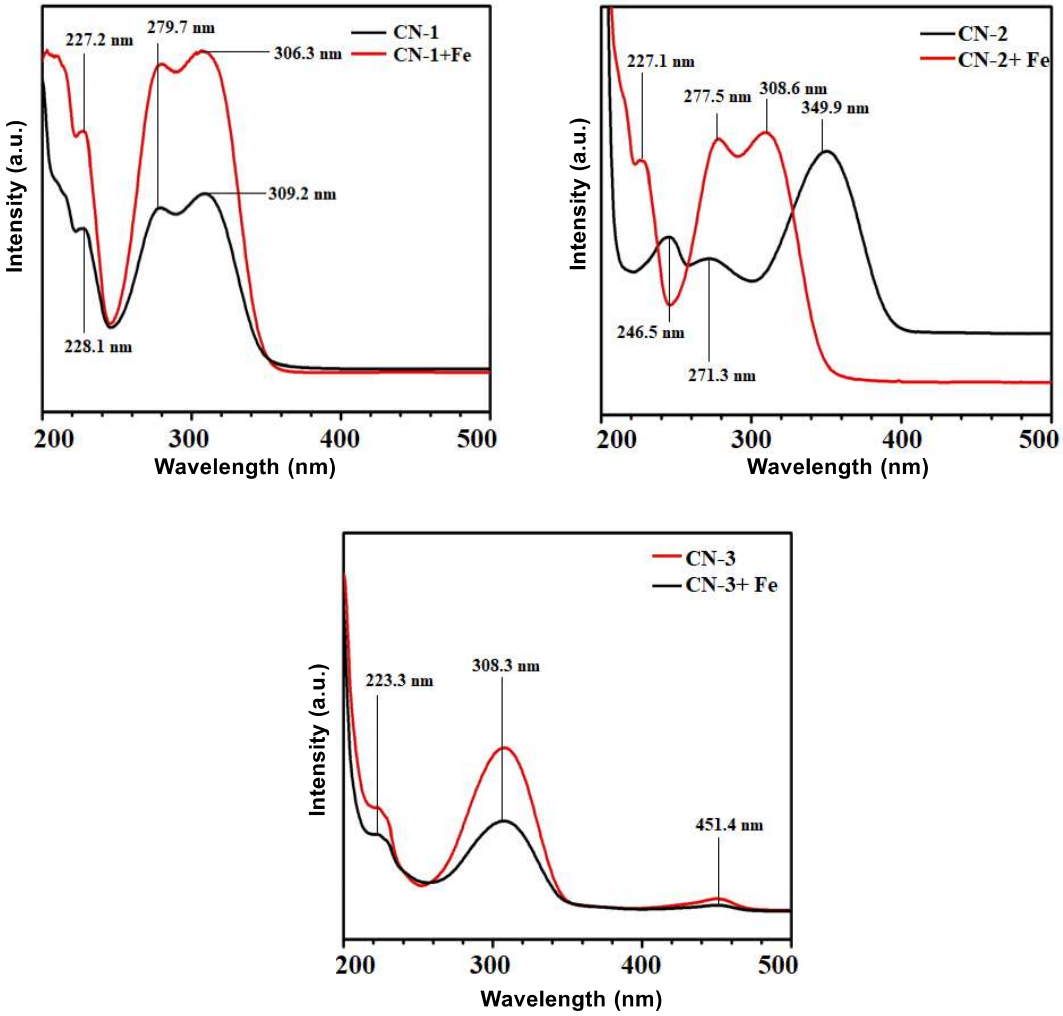

Figure 4.17: UV-visible spectra for N80 in the absence and presence of optimum concentrations of CNs in 15% HCl at 35 °C

4.2.4 Theoretical studies

4.2.4.1 Molecular modeling.

Figure 4.18 represents the optimized structures and, HOMO/ LUMO orbital density distribution for both neutral and protonated forms of inhibitors along with their corresponding orbital energies. According to the figure, the optimized structures of all

molecules show an almost planar configuration. The presence of planar geometry makes the molecules adsorb strongly over the metal surface, thus providing higher inhibition efficiencies. The HOMO and LUMO correspond to the inhibitor molecules' electron donation and acceptation ability. The studied molecules consist of both π and σ type orbitals, which help interact favorably with the metal orbitals. In the case of neutral inhibitor molecules, the HOMO for CN-1 is distributed over the phenyl and naphthyridine rings, double bond conjugation, and heteroatoms. In the CN-2 phenyl ring, the OCH_3 group, heteroatoms, and naphthyridine ring are the HOMO centers. Although, in CN-3, HOMO distribution is at the heteroatoms and naphthyridine ring. However, the LUMO distribution in CN-1, and CN-2 are almost similar to that of HOMO. Nevertheless, CN-3 LUMO distribution includes the phenyl and naphthyridine rings and heteroatoms. Since-, in the acidic medium, the inhibitor molecules undergo protonation, and the speciation graphs confirmed that. In the case of protonated forms of inhibitors for CN-1, the HOMO is distributed at phenyl and naphthyridine rings and double bond conjugation. For, CN-2 HOMO is over the entire molecule i.e. phenyl and naphthyridine rings, OCH_3, and heteroatoms. However, in CN-3, HOMO is only at the naphthyridine ring and heteroatoms. The LUMO distribution for all protonated inhibitors is over the entire molecules except in the $–NH_2$ group.

Table 4.7. Energy order of the frontier molecular orbitals of CNs.

Inhibitor (mg/L)	E_{HOMO} (eV)	E_{LUMO} (eV)	E	I	A	η	χ	Dipole moment	ΔN%
CN-1	-5.912	-2.810	3.102	5.912	2.810	1.551	4.361	10.349	0.148
CN-2	-5.994	-2.703	3.291	5.994	2.703	1.645	4.348	11.038	0.143
CN-3	-6.037	-2.604	3.433	6.037	2.604	1.716	4.320	9.320	0.145
CN-1*	-6.280	-3.248	3.032	6.280	3.248	1.516	4.764	11.691	0.108
CN-2*	-6.424	-3.259	3.165	6.424	3.259	1.582	4.841	11.975	-0.006
CN-3*	-6.60	-3.197	3.403	6.600	3.197	1.701	4.898	12.071	-0.023

* protonated.

The energy gap (ΔE) is an important descriptor to define the inhibitor molecule'sactiveness. Generally, the inhibitor molecules with lower values of ΔE have a higher potential to donate the electrons. At present, CN-1 has the lowest ΔE value in both neutral and protonated forms compared to CN-2 and CN-3, providing CN-1 a better interactioability with the iron surface.

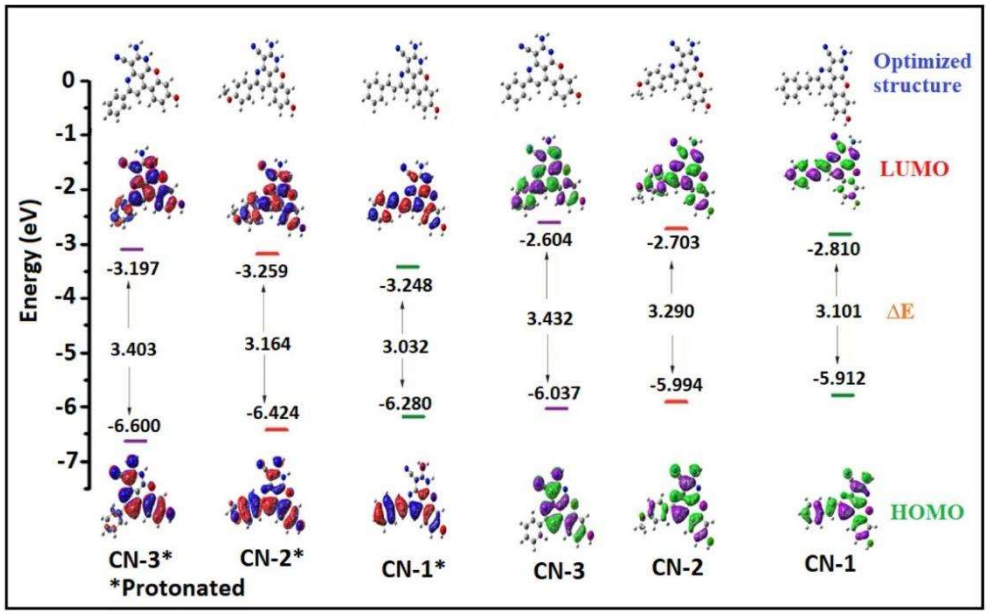

Figure 4.18. Optimized structures and, HOMO/ LUMO orbital density distribution for both neutral and protonated forms of CNs along with the orbital energy.

According to Figure 4.18, E_{HOMO} values of CNs in neutral forms are higher than in protonated forms. This reveals that the neutral inhibitor forms are having higher ability to donate the electrons to vacant iron orbitals. In the same way, the lower values of E_{LUMO} of protonated forms as compared to neutral states suggest the more ability of protonated forms to accept electrons from filled iron orbitals. In addition to this, the ΔE values of protonated forms of inhibitors are lower than the neutral forms. This suggest that the inhibitors in protonated forms are more reactive than neutral forms. Thus, the inhibitors in protonated forms have higher tendency to undergo adsorption over the N80 steel surface than there corresponding neutral forms.

In consideration of quantum chemical approach, another important parameter that elucidates the inhibition effect of the molecules is the fraction of electron transferred (ΔN) between the inhibitor molecule and the metallic surface atom. According to the Koopmans' theorem, HOMO and LUMO are associated with the ionisation potential (I) and electron affinity (A) of the molecules by the following equations [(Lukovits, Kalman, and Zucchi 2001)]:

$$I = -E_{HOMO} \quad (4.11)$$

$$A = -E_{LUMO} \quad (4.12)$$

The calculated I and A values are used to obtain the electronegativity (χ) and the global hardness (η) of the inhibitor molecules using the following equations:

$$\chi = \frac{I + A}{2} \quad (4.13)$$

$$\eta = \frac{I - A}{2} \quad (4.14)$$

The fraction of electron transferred (ΔN) between the inhibitor molecule and the metal surface is calculated by using equation 3.20.

where ηFe and ηinh are the hardness of the iron and the inhibitor molecule, respectively. The value of work function (ϕ) is 4.82. The transfer of electron from inhibitor molecule to the metallic surface will occur when $\Delta N > 0$ and vice versa [(Saha and Banerjee 2015)] have reported that there is an increase in the electron donation capability of inhibitor molecules when the ΔN value is less than 3.6 [(Awad, Mustafa, and Elnga 2010)]. From

Table 4.7, it is observed that the calculated ΔN values for neutral CNs are positive and lower than 3.6, which strongly indicates that the inhibitor molecules have the capability in donating electrons to the vacant d-orbital of metal. Hardness is another important parameter to elucidate the adsorption ability of the inhibitor molecules. On the basis of the Hard and Soft acid base principle, the metal acts as soft acid while the inhibitor molecules are considered to be soft bases [(Saha and Banerjee 2015)]. Therefore, the most crucial factor for adsorption is the soft-soft interaction between the inhibitor molecule and the metal surface. It is seen from Table 4.7 that the both in neutral and protonated forms the calculated values of hardness follow the trend CN-3>CN-2>CN-1. These results also support that CN-1 has better adsorption capability than the CN-2 and CN-3. Furthermore, from Table 4.7 it is concluded that the dipole moment of CNs both in neutral and protonated forms has higher value comparing to that of water and this indicates CNs molecules have a higher activity to adsorbed on the N80 steel surface via substitution of water molecules [(Verma *et al*. 2016)].

4.2.4.2 Molecular dynamic simulation (MDS).

The possible adsorption configuration of CN-1, CN-2, and CN-3 are depicted in Figure 4.19 a,b for both neutral and protonated forms. It is noteworthy that in all three inhibitor molecules the configuration of adsorption is parallel, which supports their strong adsorption ability over the N80 steel surface. This parallel adsorptive nature of CNs molecules causes to stop inwards flow of corrosive particles like H^+, H_2O, and Cl^- ions and thus making the metal surface safe from corrosion. Additionally, the binding energy of CNs

molecules varies with the presence of either double bond conjugation/ electron donor methoxy group/no substituent and this leads to providing different values of corrosion inhibition efficiencies of these molecules. Generally, the more the value of binding energy stronger would be the adsorption, and the higher would be the corrosion inhibition efficiency.

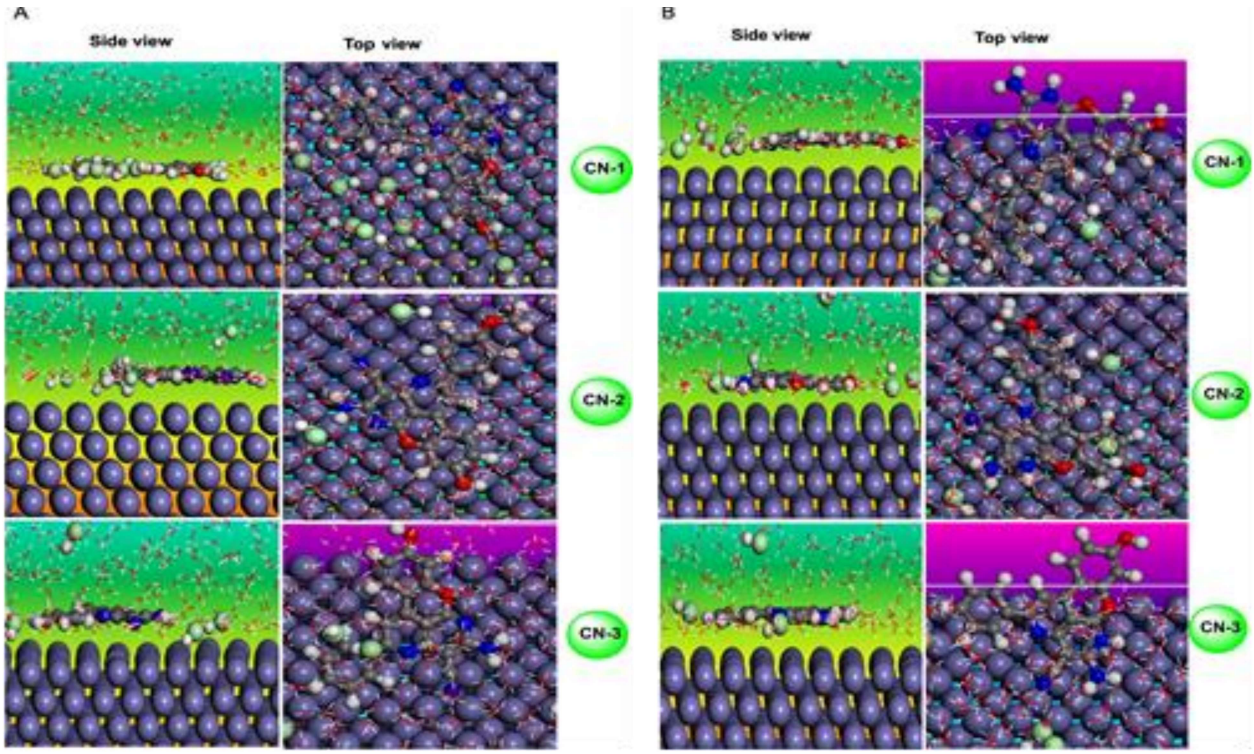

Figure 4.19 **a**. Side and top views of the final adsorption of neutral forms of CNs on Fe (110) surface. **b**. Side and top views of the final adsorption of protonated forms of CNs on Fe (110) surface.

In the present case, the binding energy ($E_{binding}$) are in the following order: CN-1 (−870.71 kJ/mol) > CN-2 (−737.79 kJ/mol) > CN-3 (−700.46 kJ/mol) for neutral forms and CN-1 (−813.46 kJ/mol) > CN-2 (−650.05 kJ/mol) > CN-3 (−625.37 kJ/mol) for protonated forms.

Thus, the highest value of binding energy was obtained for CN-1 both in neural and protonated forms.

4.2.5 Mechanism of corrosion and inhibition.

Corrosion is an electrochemical process that involves anodic and cathodic reactions. The mechanism of iron dissolving at the anodic site in HCl solution is depicted below. equations 4.3 – 4.6: According to the result of PDP, the CNs is, a predominantly anodic inhibitor and thus protonated form of inhibitor (CNsH+), predominantly adsorbed on anodic site as follows:

$$(FeCl^{-})_{ads} + CNsH^{+} \rightarrow (FeCl^{-}CNsH^{+})_{ads} \quad (4.15)$$

Therefore, the protonated inhibitor ($CNsH^{+}$) from Eq. (20) can electrostatically adsorb on the surface of the metal and block the anodic reaction .

Likewise, the cathodic reaction mechanism is follows equations 4.8-4.10:

The protonated inhibitor molecules can also adsorb at cathodic sites, reducing hydrogen evolution. The $\Delta G°_{ads}$ data show a mixture of chemical and physical adsorption mechanisms. Furthermore, E values indicate that the inhibitors in protonated ($CNsH^{+}$) forms have greater interaction ability than neutral forms. The inhibitor compounds are chemically adsorbed by giving their electron pairs (present in phenyl rings and/or heteroatoms) to the vacant iron orbitals [(Eduok, Ohaeri, and Szpunar 2018)]. The adsorption mechanism is shown in Figure 4.20. The differences in inhibitory efficacy of the three CNs derivatives can be explained by differences in their structural characteristics. Because of the presence of the electron-donating $-OCH_3$ group, the CN-2 performs better

than the CN-3. In the instance of CN-1, the presence of a conjugated double bond offers the highest inhibitory efficacy when compared to other inhibitors (CN-2 and CN-3). The experimental findings were strongly supported by the theoretical investigations.

Figure 4.20 Inhibition mechanism of CNs adsorption on N80 steel surface.

4.2.6 Conclusion.

1. CN-1 had the best corrosion inhibitor performance among the three inhibitors. All CNs' inhibitory efficiency improves with concentration and decreases with temperature.

2. The Gibbs adsorption free energy confirms the spontaneous and heterogeneous character of CNs adsorption. In AFM, a decrease in average roughness (Ra) in the presence of CNs compared to blank indicates that CNs molecules have adsorbed onto the N80 steel surface and function as a barrier between the N80 steel surface and the corrosive medium.

3. The removal of stretching bands of N-H, aromatic C-H, CN, and C=C in FTIR suggests that they are actively engaging in the adsorption process, which results in the creation of a CNs molecular film over the N80 steel surface.

4. UV-vis indicates the development of a compound between Fe^{2+} and CNs molecules and confirms the suppression of corrosion in N80 steel.

5 The DFT measurements show that corrosion is inhibited by the adsorption of both neutral and protonated inhibitors.

6. The parallel adsorption of CNs molecules in neutral and protonated states is suggested by molecular dynamic simulation (MDS).

7. The inhibitors were produced utilising less hazardous compounds, green solvents (such as water), and reusable catalysts (such as silica gel), proving that all of the inhibitors are ecologically friendly corrosion inhibitors.

4.3 Quinoline Carbonitriles as Novel Inhibitors for N80 Steel Corrosion in Oil-Well Acidizing.

N80 steel is one of the most preferred structural materials for application in the petroleum industry. Acidizing process carried out in the oil and gas sector involves the application of concentrated hydrochloric acid (typically 15–28%) for dissolving the mineral encrustations and improving oil recovery [(Quraishi, Chauhan, and Saji 2020; Ansari *et al*. 2020; Schmitt 1984)), Ansari *et al*. (2020), Schmitt *et.al*. (1984)]. The highly concentrated acidic solution causes severe corrosion of the steel structures resulting in a substantial economic loss and hazards of potential structural failure. To circumvent this issue, it is a common practice to inject corrosion inhibitors in the acid solutions, which adsorb the steel structures and minimize the corrosion damage. Thus the use of organic heterocyclic corrosion inhibitors offers the advantage in terms of the presence of (i) heteroatoms (N, S, O), (ii) π bonds, (iii) phenyl rings, and (iv) functional groups, which together impart a superior capability of adsorption on the metallic surface [(Quraishi, Chauhan, and Saji 2020; Ansari *et al*. 2020; Schmitt 1984)].

Quinolines are one of the most common constituents of pharmaceutical products. Quinoline and its functionalized derivatives are reported as corrosion inhibitors in a number of studies [(Cicileo *et al*. 1998; Ebenso, Obot, and Murulana 2010; Verma *et al*. 2016; Jiang *et al*. 2018)]. We, for the first time, present the influence of three quinoline derivatives, namely 2-amino-7-hydroxy-4- phenylquinoline-3-carbonitrile (AHQ-1), 2-amino- 7-hyrbonitrile (AHQ-2) and (E)-2-amdroxy-4-(4- methoxyphenyl) quinoline-3-

caino-7-hydroxy-4-styrylquinoline- 3-carbonitrile (AHQ-3) on corrosion inhibition of N80 steel in 15% HCl. The significant benefit of these derivatives is the presence of the –OH, –NH_2, and the –CN functional groups along with the additional phenyl ring containing the –OCH_3 group (AHQ-2) and the additional double bond (AHQ-3). Therefore, these inhibitor molecules have a large size that can adequately cover a considerable area of the steel surface, and the presence of additional structural features in terms of the multiple functional groups can aid in the adsorption Another feature of these inhibitors is that they are prepared via a single step multicomponent reaction (MCR). This approach is a modern technique, in which instead of adding the different reactants together in a step-wise procedure, all the reactants are added together to achieve the desired product in a single step. Furthermore, the synthesis of the inhibitors was performed in a microwave reactor in the aqueous medium, which avoided the use of any toxic organic solvent, and the entire synthesis was carried out within 10 min. The corrosion evaluation was carried out in 15% HCl using weight loss studies, impedance spectroscopy, electrochemical frequency modulation, and polarization measurements supported with scanning electron microscopy and FTIR. Theoretical estimation of the reactivity indices was carried out by the pKa analysis, DFT studies, and Monte Carlo simulations.

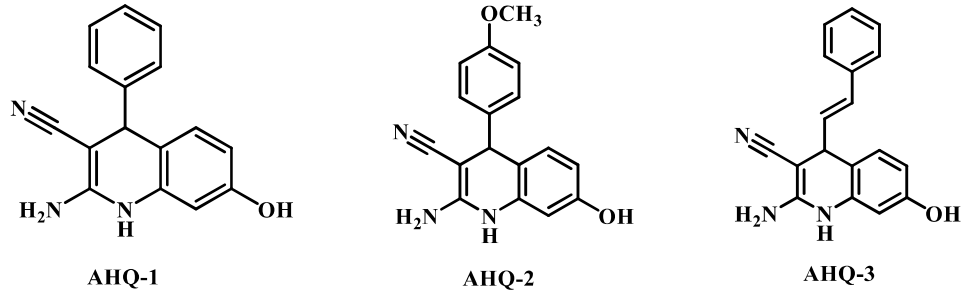

Figure 4.21 Structure of inhibitors: AHQ-1, AHQ-2, AHQ-3

4.3.1 Gravimetric Studies.

4.3.1.1 Influence of inhibitor concentration.

The weight loss measurements provide a simple and reliable method of analyzing the corrosion inhibition performance of newly developed inhibitor molecules [Baboian *et al.* (2005)]. The N80 steel specimens were dipped in the corrosive solution of 15% HCl, and the weight loss studies were carried out without and in the presence of the inhibitors. The quinolines were added to the corrosive solution in the range of 50 to 400 mg L^{-1}, and the obtained data is displayed graphically in Figure 4.22a. The inhibition efficiency rose with an increase in the inhibitor dose in all three cases and attained a value of 97.5% for the AHQ-3 derivative containing the cinnamaldehyde moiety. The order of the inhibition efficiency for the three inhibitors varied from R = –H < R = –OCH_3 < R = –$CH{=}CH_2$. The higher efficiency in the case of the –OCH_3 derivative compared to that in the –H derivative is ascribed to the electron-donating effect of the methoxy group. The introduction of the π bond conjugation in the cinnamaldehyde derivative is ascribed to the observed highest inhibition efficiency of the inhibitor AHQ-3. The improvement in the efficiency with the inhibitor concentration shows that the quinoline derivatives adsorb on the N80 steel surface

and cover the available active sites to undergo corrosion. This considerably reduces the corrosion damage of the N80 steel surface and provides high efficiency.

4.3.1.2 Temperature effects on the adsorption behavior of inhibitors.

The oil-well acidizing industry requires the use of considerably high temperatures. Therefore, it is important for a corrosion inhibitor to show effectiveness. adsorption and inhibition behavior at high testing temperatures. However, the temperature is an essential factor that can significantly influence the nature of the adsorption of a corrosion inhibitor on a given metallic surface. In many cases, it has been a common observation that an elevation in the temperature shifts the adsorption-desorption equilibrium in the direction of the desorption. This can be attributed to the disappearance of weak physical interactions taking place between a corrosion inhibitor and a metal surface at higher temperatures. Considering the above, the adsorption of the quinoline derivatives was tested in the temperature range of 308 to 338 K in the present study using the weight loss method. At each of the temperatures, the same tests were undertaken without the inhibitors and the results of the effect of temperature are plotted graphically in Figure 4.22b. The results show that unlike most of the available literature, which reports a decline in the inhibition efficiency of the corrosion inhibitors with a rise in the temperature, in the present investigation, the inhibition efficiency remains almost constant at each of the tested temperatures for the three inhibitors. This behavior is generally attributed to a strong metal-inhibitor interaction.

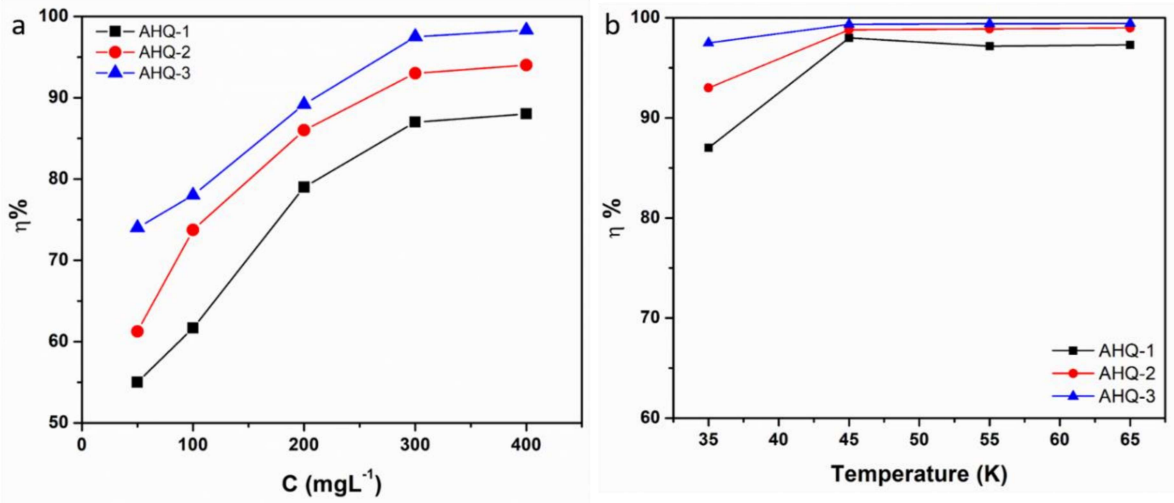

Figure 4.22 (a) Effect of variation in the concentration of the quinoline derivatives on the corrosion inhibition efficiency at 308 K. **(b)** Effect of variation in solution temperature on the inhibition efficiency at 300 mg L^{-1} dose of inhibitors.

4.3.1.3 Adsorption isotherm.

The nature of the metal-inhibitor interactions can be elucidated by using a suitable adsorption isotherm. The obtained weight loss data for the three quinoline derivatives were plotted to fit several different isotherms. Among these, the most suitable fit was observed in the Langmuir isotherm, which can be described in equation 4.1:

Where the term K_{ads} represents the equilibrium constant for adsorption, and *c* symbolizes the inhibitor concentration. The plots of Langmuir adsorption isotherm for the three quinoline derivatives are shown in Figure. 4.23. The slope and the regression coefficient are close to unity supporting the validity of the fitting. The adsorption free energy (ΔG^0_{ads}) can be equated with the equation 3.13:

Where the term 55.5 denotes the concentration of water in mol L^{-1}. From the plots of the Langmuir isotherms, the values of the K_{ads} were determined using the intercepts. Using these values, the values were calculated to be –31.15, –32.24, and –32.92 kJ mol^{-1}, for AHQ-1, AHQ-2, and AHQ-3 respectively.

The negative sign is indicative of the spontaneity of the adsorption process. The obtained free energy values suggest that the inhibitor adsorption on the steel surface obeys mixed physical and chemical adsorption.

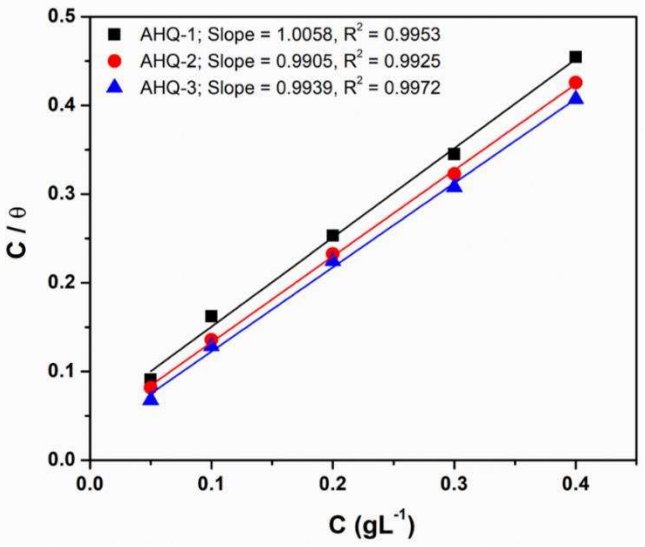

Figure 4.23 Plots of Langmuir isotherm for the adsorption of the three inhibitors on N80 steel surface in 15% HCl.

4.3.2 Electrochemical studies.

4.3.2.1 Electrochemical impedance spectroscopy.

The impedance measurements provide a non-destructive and straightforward means to characterize the metal/solution interfaces [Solmaz *et al*. (2014), Solmaz *et al*. (2008)]. A

suitable frequency range is applied according to which the response is observed in the form of the real and imaginary impedances (Nyquist plots) or the variation as a function of the logarithm of the applied frequencies vs. either the phase angle (phase plots) or the impedance modulus (the Bode plot). The different concentrations of the three quinoline derivatives were introduced to the 15% HCl electrolyte, and the obtained response was plotted in terms of the Nyquist plot, as shown in Figure 4.24. The equivale circuit diagram employed for fitting the EIS data is shown in Figure 4.24. The electrochemical parameters were obtained and are shown in Table 4.8. The description of the different electrical elements used in the circuit diagram is given elsewhere. A noteworthy feature of the Nyquist plots is the appearance of the depressed capacitive semicircles instead of the ideal semicircles, which represent the frequency distribution behavior commonly observed in the case of a corroding metal surface immersed in corrosive acidic electrolytes. In such cases, instead of an ideal double-layer capacitor, a constant phase element is applied to obtain accurate modeling of the frequency distribution behavior [(Popova and Christov 2006; Popova *et al*. 2004)]. The equation 3.5 can give the impedance of the CPE: Where Y_0 denotes a coefficient of proportionality, ω is the angular frequency, n is the CPE exponent with values between 0 and 1, and provides a gauge for the surface heterogeneity [(Chauhan *et al*. 2019)]. Table 4.8 shows the calculated electrochemical parameters, along with the corrosion inhibition efficiencies. The diameter of the Nyquist semicircles increases successively with the addition of the inhibitor in the successively increasing concentrations.

This behavior can be connected with a thickening of the inhibitor film formed at the metal/solution interface, which could be quantified in terms of the observed increase in the charge transfer resistance (R_{ct}) values. The corrosion inhibition efficiency was obtained using the R_{ct} values, as shown in equation 3.7.

Where, R_{ct} and R_{ct}^{inh} denote the charge transfer resistances without and containing the inhibitor, respectively. The R_{ct} values increased with the inhibitor dosage and attained considerably high values of 160.7, 263.0, and 359.6 Ω cm^2 for the case of AHQ-1, AHQ-2, and AHQ-3 at a dosage of 300 mg L^{-1}. This corresponds to high inhibition efficiencies of 96.6, 97.9, and 98.4%, respectively. The rise in the charge transfer resistance with the inhibitors is attributable to the inhibitor adsorption, which increases the inhibition efficiency. The double-layer capacitance (C_{dl}) was evaluated by equation 3.6.

Corresponding to the increase in the R_{ct} values, the C_{dl} values showed a continuous decrease upon the addition of successive inhibitor concentrations, as shown in Table 4.8. A decline in the observed values of the C_{dl} can be ascribed to a lowering in the local dielectric constant, which could be connected with the replacement of the water molecules that are already adsorbed on the metal surface by the organic corrosion inhibitor molecules [Ozcan *et.al*. (2004)]. This shows that the inhibitors adsorb on the metal/electrolyte interface at the active sites and decrease the values of C_{dl}.

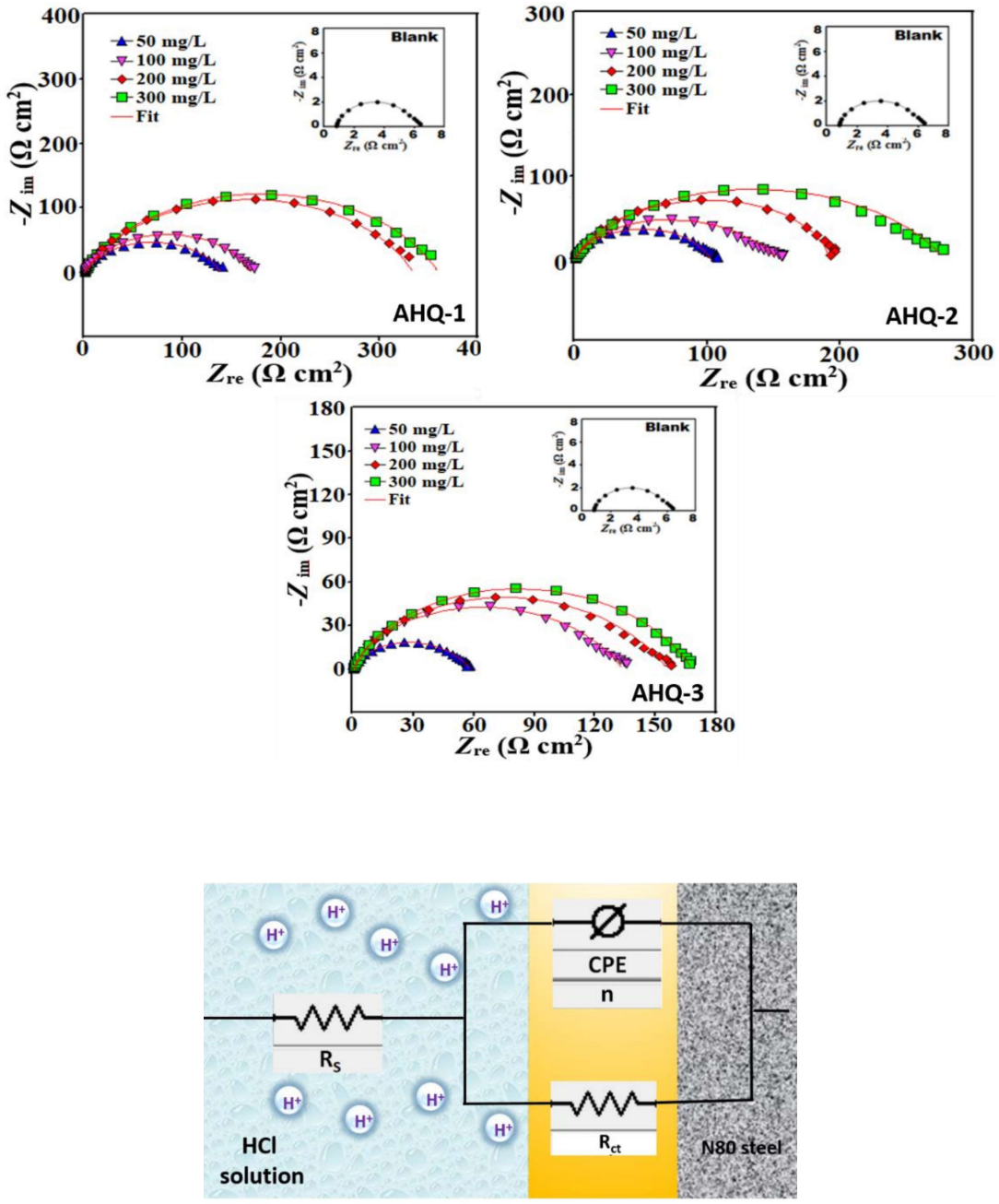

Figure 4.24 Experimental and simulated Nyquist plots for the adsorption of the three quinoline derivatives on N80 steel surface in 15% HCl.

Table 4.8. Electrochemical impedance parameters of N80 steel in 15% HCl at different concentrations of AHQs at 308 K.

Cinh (mg/L)	R_s (Ω)	R_{ct} (Ω cm^2)	Y_0 (μF/cm^2)	n	C_{dl} (μF/cm^2)	η (%)
Blank	0.82	5.404	406	0.755	72.1	
AHQ-1						
50	0.532	57.1	255	0.757	65.6	90.5
100	0.066	126.9	180	0.765	53.3	95.7
200	0.589	147.2	136	0.799	49.9	96.3
300	0.529	160.7	136	0.815	35.87	96.6
AHQ-2						
50	0.67	101.4	211	0.767	67.1	94.6
100	0.722	142.7	147	0.783	60.5	96.2
200	0.686	190.5	92	0.815	52.9	97.1
300	0.550	263.0	74	0.832	45	97.9
AHQ-3						
50	0.582	137.8	159	0.781	69	96.0
100	0.550	173.4	113	0.798	65.9	96.8
200	0.721	334.2	67	0.825	57.6	98.3
300	0.646	359.6	55	0.85	54.2	98.4

4.3.2.2 Potantiodynamic polarization studies.

Corrosion of steels in acidic environments involves two electrochemical processes: (i) dissolution of Fe metal at the anodic sites, and (ii) reduction of the H^+ ions and the evolution of the gaseous hydrogen at the cathodic sites. In this context, the Potentiodynamic polarization (PDP) measurements provide valuable information upon the electrochemical kinetic behavior of a corroding system [McCafferty *et.al.* (2010)]. Therefore, in the present study, the three quinoline derivatives were added to the corrosive

electrolyte of 15% HCl in varying concentrations, and the polarization measurements were performed. The anodic and cathodic Tafel curves were plotted to meet at their point of intersection from where the electrochemical parameters and the corrosion current densities were computed. The results of the PDP analysis are displayed in Figure 4.25. The electrochemical parameters are given in Table 4.8, and the inhibition efficiency was computed as equation 3.8.

Where the symbols 'b' and 'i' respectively denote the blank and the inhibited samples. The addition of the quinoline-based corrosion inhibitors to 15% HCl produced a significant decrement in the corrosion current densities (i_{corr}) of both the anodic/cathodic Tafel curves. The i_{corr} values of the N80 steel sample decreased significantly from 1630 μA cm^{-2} in the case of the blank sample to 61, 42, and 38.1 μA cm^{-2} in the presence of the AHQ-1, AHQ-2, and AHQ-3 inhibitors, respectively. The lowering of the i_{corr} values corresponds to high corrosion inhibition efficiencies of 96.2, 97.3, and 97.6% in cases AHQ-1, AHQ-2, and AHQ-3, respectively. This suggests that the quinoline derivatives retarded both the anodic and the cathodic processes of corrosion and is suggestive of a mixed type inhibitor action of the quinoline derivatives.

Further, a different shift in the corrosion potential (E_{corr}) could be visualized with the successive addition of the higher concentrations of inhibitors. This indicates that the inhibitors shift the corrosion potential towards a positive direction concerning the E_{OCP}. However, the observed shift is not significant enough to categorize the electrochemical corrosion inhibition process as a purely anodic type, and it supports a mixed type

mechanism with the prevalence -of cathodic control. Also, the slope values of the anodic and the cathodic electrochemical processes do not show a noticeable change upon the adding corrosion inhibitors. This shows that the addition of the quinoline derivatives to the corrosive electrolyte does not bring about any change in the mechanism of corrosion. The observed corrosion inhibition efficiencies follow the trend $–CH=CH_2$ > $–OCH_3$ > –H, which supports the results obtained above in the gravimetric and the EIS data.

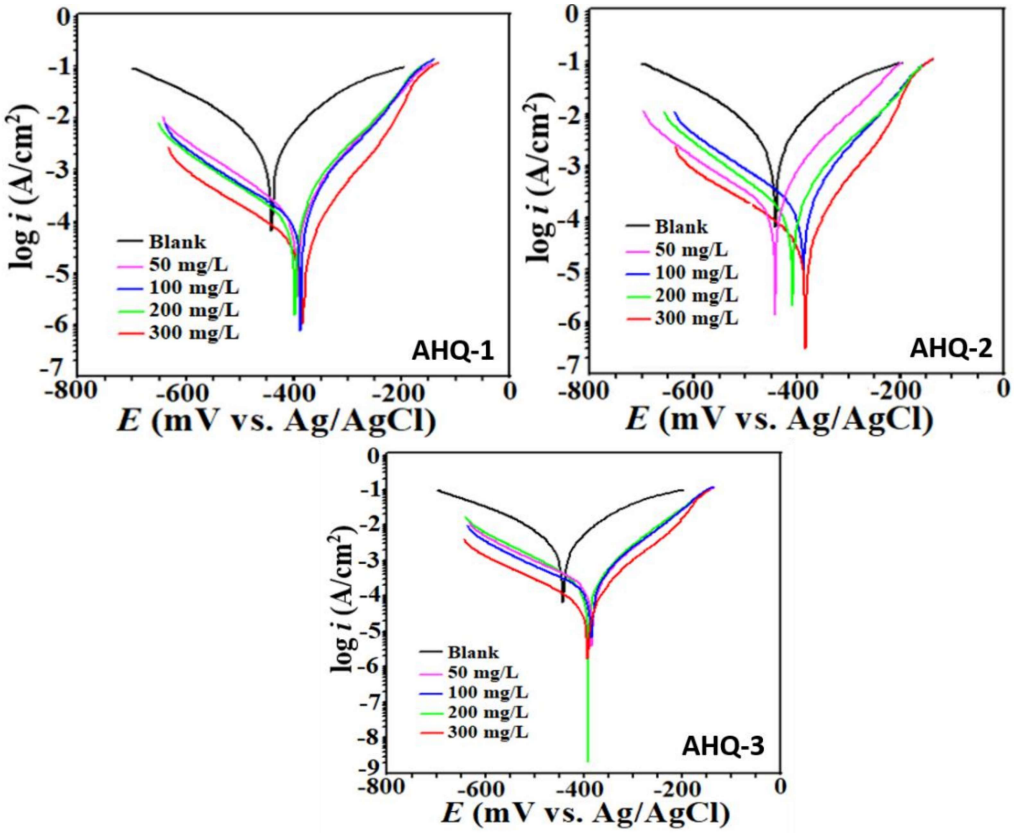

Figure 4.25. Potentiodynamic polarization curves recorded for the adsorption of the three quinoline derivatives on N80 steel surface in 15% HCl.

Table 4.9. Electrochemical polarization parameters of N80 steel in 15% HCl at different concentrations of AHQs at 308 K.

Inhibitor conc. (mg/L)	E_{corr} (mV/SCE)	i_{corr} ($\mu A/cm^2$)	β_a (mV/dec)	$-\beta_c$ (mV/dec)	η (%)
Blank	-443	1630	86	101	
AHQ-1					
50	–383	272	88.2	231.9	83.3
100	–386	262	85.4	356.6	83.9
200	–391	160	71.5	120.1	90.1
300	–392	61	72.3	161.7	96.2
AHQ-2					
50	–443	211	73.5	233.4	87.0
100	–388	202	81.5	184.6	87.6
200	–409	158	79.5	173.8	90.3
300	–384	42	71.6	169.9	97.3
AHQ-3					
50	-394	162	76.3	165.6	90.0
100	-388	149	71.3	235	90.8
200	-398	139	69.9	290.4	91.4
300	-384	38.1	68.7	157.1	97.6

4.3.3 Surface Analytical Measurements.

4.3.3.1 Scanning electron microscopy (SEM).

The morphology of the N80 steel substrate after immersion in the 15% HCl without and in the presence of the quinoline derivatives was studied using scanning electron microscopy. The results shown in Figure 4.26 depict a considerably damaged N80 steel surface showing a number of pits, striations, and rough surfaces. It can be observed that the surface of the

N80 steel displays a considerable improvement in morphology, supporting the protective performance of the three inhibitors. This can be assigned to the formation of a protective inhibitor film on the metallic surface that provides isolation from the corrosive attack of the acid [(Singh *et al*. 2019)].

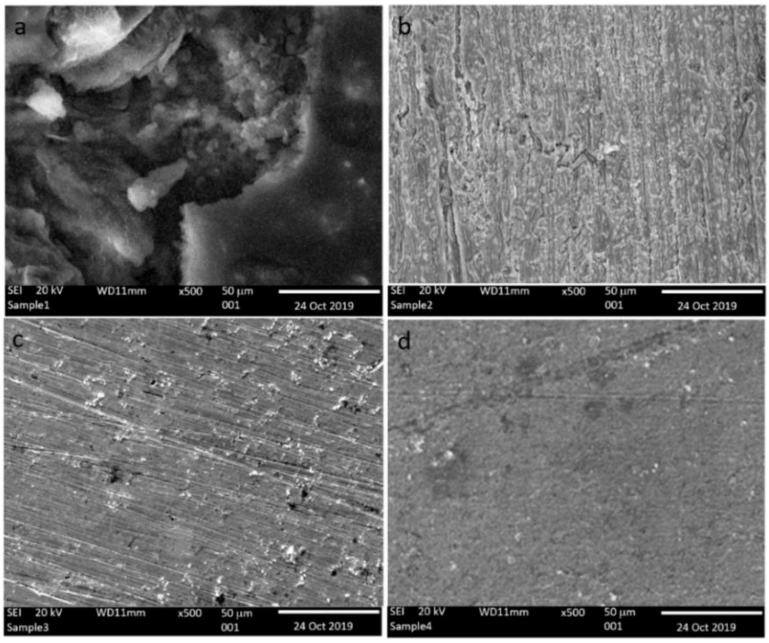

Figure 4.26 SEM images of the N80 steel surface after immersion for 24 h in 15% HCl in the absence of corrosion inhibitor **(a)**, and in the presence of 300 mg L^{-1} concentration of AHQ-1 **(b)**, AHQ-2 **(c)**, and AHQ-3 **(d)**.

4.3.3.2 FTIR measurements.

The FTIR analysis is a convenient means to obtain a piece of concrete information on the adsorption of the corrosion inhibitors on a given metallic surface and the formation of a smooth inhibitor film [(Singh *et al*. 2019; Chauhan *et al*. 2019)]. The FTIR measurements were performed to study the inhibitor adsorption on the metallic surface, and the results are

shown in Figure 4.27. The presence of the FTIR signals characteristic to the quinoline derivatives on the N80 steel surface matching the data shown and provide supporting evidence for the inhibitor adsorption on the metal surface.

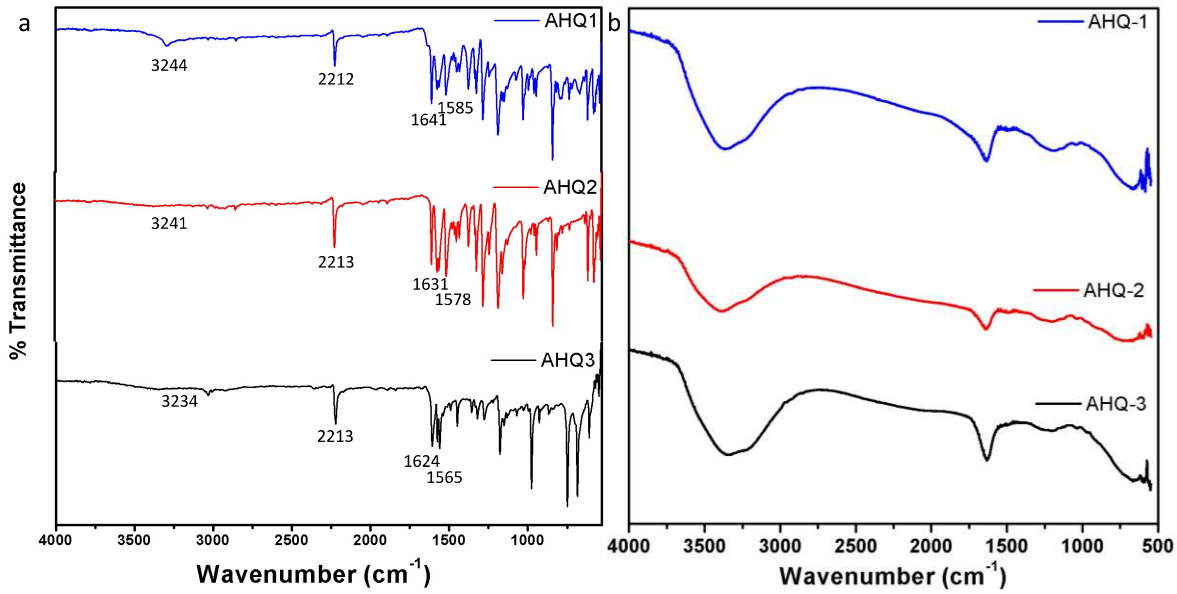

Figure 4.27 (a) FTIR spectra of the three quinoline derivatives; **(b)** FTIR spectra of the quinoline derivatives recorded on the N80 steel surface following an immersion period of 24 h.

4.3.4 Theoretical study

4.3.4.1 Computational Studies.

A corrosion inhibitor molecule, when placed in an acidic solution, is likely to undergo protonation. Therefore, the analysis of the possible sites that are amenable to undergo protonation in a corrosive environment becomes an essential aspect of computational studies. The p*K*a analysis of the three quinolines was performed, and the

results are displayed in Figure 4.28. It can be observed that at the three inhibitor molecules show a tendency to undergo protonation at the pyridine N.

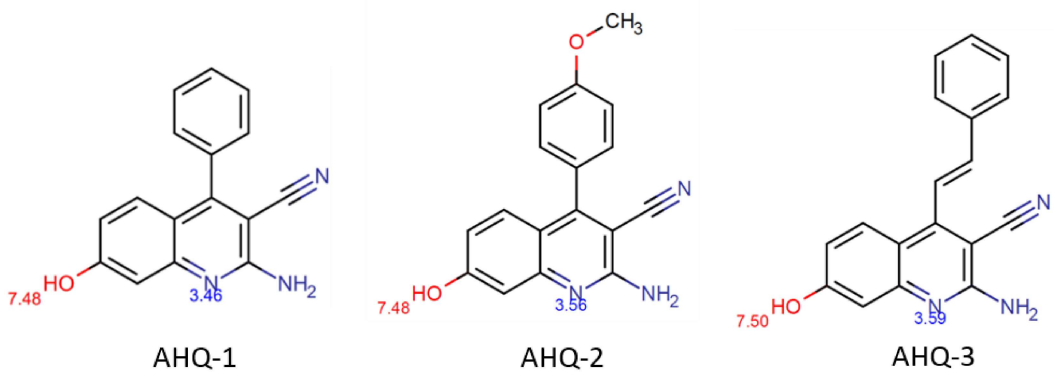

Figure 4.28 Calculated p*K*a values of the three quinoline derivatives.

In corrosion inhibition studies, the theoretical estimation of the reactivity is usually carried out to understand the correlation between the structure and the adsorption and inhibition of the corrosion inhibitors [(Dohare *et al*. 2017)]. The results of the calculations provided the frontier molecular orbital (FMO) energies based on which the different reactivity parameters were calculated, as shown below. The optimized structures and the molecular orbital distributions of the three corrosion inhibitors (neutral forms) are given in Figure 4.29, and the calculated quantum chemical parameters are shown in Table 4.10. In the optimized geometry of the inhibitor molecules, the quinoline ring shows a flat orientation, whereas the phenyl ring is out of the plane.

Table. 4.10 Calculated quantum chemical parameters of quinoline derivatives in the neutral form

Component	E_{HOMO}	E_{LUMO}	ΔE	χ	η	σ	ω	ε	ΔN	Component
AHQ-1	-5.6850	-1.8784	3.81	3.78	1.90	0.53	1.88	0.53	0.27	AHQ-1
AHQ-2	-5.5589	-1.7603	3.83	3.68	1.91	0.52	1.76	0.56	0.29	AHQ-2
AHQ-3	-5.3990	-2.3089	3.09	3.85	1.55	0.65	2.40	0.42	0.31	AHQ-3

This shows that the Nitrogen atoms of the quinoline ring and the –OH, $–NH_2$, and the –CN groups exhibit a high tendency to undergo adsorption on the metallic substrate by sharing of electrons. The energy of the molecular orbitals was obtained from the calculations and was used to calculate the ionization potential (I) and the electron affinity (A):

The electronegativity (χ), hardness (η), and the global softness (σ) were calculated using equations 4.11-4.14.

The electrophilicity index is an important reactivity parameter that provides a measure of the electron-donating capability of a corrosion inhibitor molecule. The electrophilicity index (ω) and its inverse the nucleophilicity index (ε) can be defined as follows.

$$\omega = \frac{\mu^2}{4\eta} = \frac{\chi^2}{4\eta} \qquad (4.16)$$

$$\varepsilon = \frac{1}{\omega} \qquad (4.17)$$

The fraction of electrons transferred between inhibitor molecules and the metal surface can be calculated as equation 3.20.

Where, χ_{metal} and χ_{inh} show the absolute electronegativities of the metal and inhibitor respectively and η_{metal} and η_{inh} are the hardness values of the metal and inhibitor, respectively. Here it should be noted that the value of ΔN does not exactly denote the actual

number of electrons transferred, and it is merely indicative of the "electron-donating ability." To calculate the fraction of electrons transferred between inhibitor and the metal, a theoretical value of 7 eV for χ_{Fe} of bulk iron and a global hardness $\eta_{Fe} = 0$ is used considering I=A for bulk metal [Kokaji *et al*. (2012), Kokaji *et al*. (2011)]. [Kokaji *et al*. (2010)] have shown that the use of the work function of metal (Φ_{Fe}) instead of χ_{Fe} is more appropriate for an adsorbate–metal surface interaction. Thus, using (Φ_{Fe}) in place of χFe and taking $\eta_{Fe} = 0$, the equation 3.20 becomes

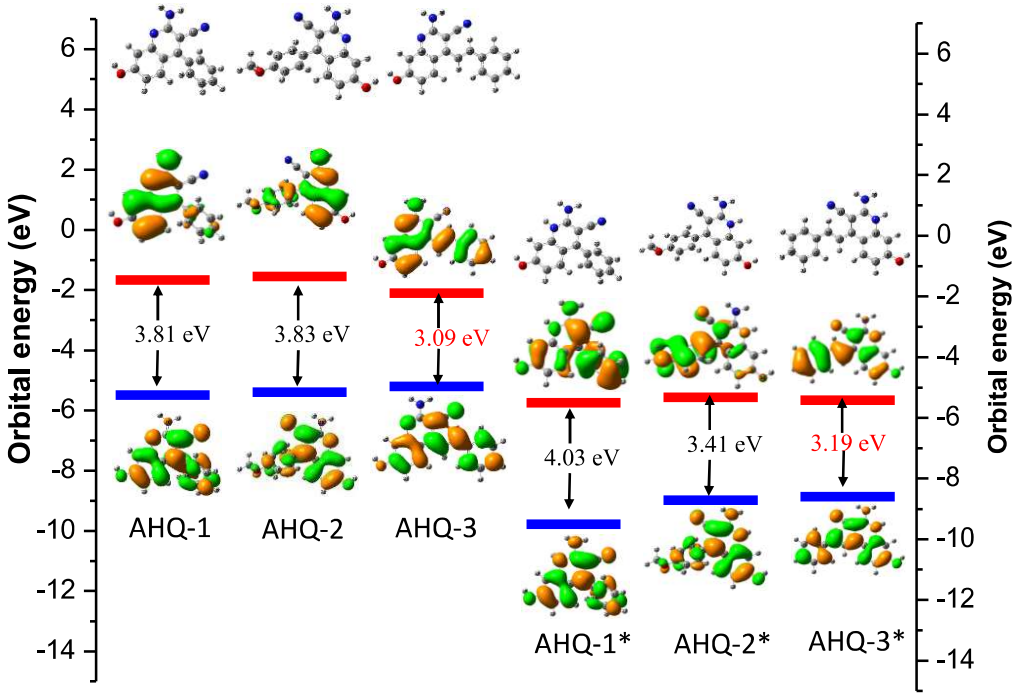

Figure 4.29 Optimized molecular structures and the molecular orbital electron density distributions of the three quinolines in the neutral and protonated **(*)** form.

$$\Delta N = \frac{\Phi_{Fe} - \chi_{inh}}{2\eta_{inh}} \quad (4.18)$$

The DFT derived values for Fe (100), Fe (110), and Fe (111) surfaces are 3.91, 4.82, and 3.88 eV, respectively. We have chosen the Fe (110) surface considering its higher stabilization energy and packed surface [(Guo *et al*. 2017)]. The transfer of electrons from the inhibitor molecule to the metallic surface will take place when $\Delta N>0$ and vice versa [(Kokalj 2012)].

Table 4.11 Adsorption parameters of AHQ-3 neutral and protonated as evaluated from the Monte Carlo simulations (all energy values in kcal mol^{-1})

Component	Total energy	Adsorption energy	Rigid adsorption energy	Deformation energy
AHQ-3 neutral	–46.4923	–6.14	–6.23	0.0835
AHQ-3 protonated	–47.6920	–6.38	–6.47	0.0852

The high value of E_{HOMO} for an organic molecule and a low E_{LUMO} value can be correlated with a higher inclination to electron donation and acceptance, respectively. From the Table, it is inferred that the inhibitor AHQ-3 denotes the highest E_{HOMO} (–5.3996 eV) value, followed by the inhibitors AHQ-2 (–5.5898 eV) and AHQ-1 (–5.6850 eV). This shows that the inhibitor AHQ-3 exhibits the highest propensity of electron donation. The energy gap of the inhibitors was the lowest in the case of the inhibitor AHQ-3. The electronegativity was found to be the highest in case of AHQ-3. The global hardness is considered as the resistance barrier to be overcome for the electron transfer to take place. Also, from the

HSAB principle, a hard molecule possesses a large energy gap and is indicative of a stable molecular structure [(Baig *et al*. 2019; Haque *et al*. 2018; Ituen *et al*. 2019) Onyeachu *et al*. (2019)]. In the present case, it can be observed that in addition to the lowest energy gap, the AHQ-3 inhibitor molecule shows the lowest value of chemical hardness and the highest value of global softness. The high softness value is correlated with a high reactivity in an inhibitor molecule. The lowest value of the electrophilicity index and highest nucleophilicity support the highest propensity of electron donation in the case of AHQ-3 compared to the other two inhibitors. The fraction of electrons transferred is also the highest in the AHQ-3 molecule, suggesting its highest inclination towards electron donation to the metal surface. Therefore, the observed trends in the quantum chemical calculations support the experimental observations that the inhibitor AHQ-3 shows the highest reactivity.

The optimized geometries and the HOMO/LUMO distributions of the three inhibitors in the protonated form are depicted in Figure 4.29, and the calculated reactivity parameters are given in Table 4.11. The values of the E_{HOMO} and the E_{LUMO} are decreased after protonation. The lowering in the E_{HOMO} values after protonation suggests a decrease in the tendency to donate electrons compared to the neutral form of the inhibitors. The decline in the E_{LUMO} after protonation suggests that the inhibitor molecules exhibit an increase in the tendency to accept the electrons compared to their neutral forms. Again, it is seen that the energy gap is the lowest for AHQ-3, which supports its highest reactivity, even in the protonated form. Besides, the global hardness is the lowest, and the global softness value is

the highest in inhibitor AHQ-3, which supports its better reactivity compared to the other two inhibitors. In the protonated form also, from the values of the energy gap, global hardness, and the global softness values, it can be observed that the trend in the inhibition efficiencies is AHQ-3 > AHQ-2 > AHQ-1 which supports the experimental observations.

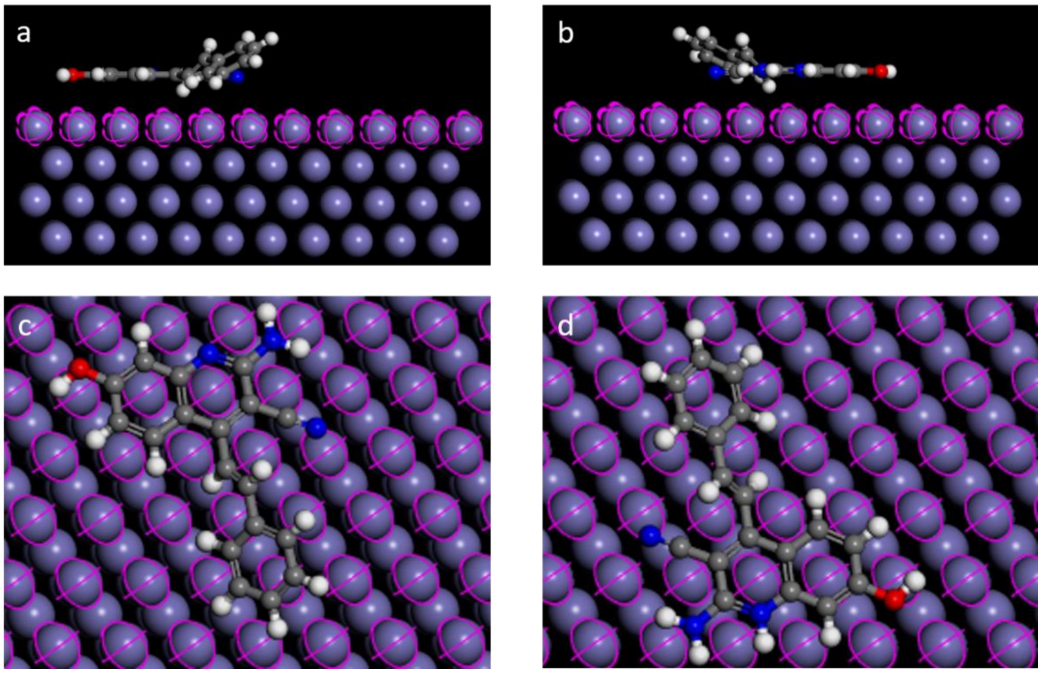

Figure 4.30 Side **(a, b)** and corresponding top **(c, d)** views of the most stable configurations for the adsorption of AHQ-3 neutral and protonated on Fe (110) surface.

To obtain deeper insight into the comparison between the neutral and protonated forms of inhibitor, we chose AHQ-3 and performed the Monte Carlo simulation study to obtain the preferred adsorption orientations on the Fe (110) surface. The Fe (110) surface was selected because this plane occupies >60% area of the Fe crystal surface. Compared to Fe (111) and Fe (100), the Fe (110) plane is a densely packed structure with higher stabilization. The

adsorption orientations of the AHQ-3 in neutral and protonated forms are shown in Figure 4.30. The adsorption energy refers to the energy released or absorbed when the relaxed inhibitor molecules are adsorbed on the metallic surface. It can also be defined as the sum of the rigid adsorption energy and the deformation energy for the adsorbed components [(Obot *et al.* 2015)]. The rigid adsorption energy refers to the energy required or released when the unrelaxed inhibitor molecules (i.e., prior to the geometry optimization step) are adsorbed on the metal surface. The deformation energy refers to the energy released when the inhibitor molecules are relaxed on the adsorbed surface. The data in Table 4.11 shows that the values of the adsorption energy are negative, which suggests strong and spontaneous adsorption of the inhibitor. These observations are in agreement with the data obtained from the p*K*a analysis and that of the DFT calculations. Larger total energy and the adsorption energies in the protonated form of AHQ-3 support its better action in this state.

4.3.5 Inhibition Mechanism.

The mechanism of inhibition in the presence of quinoline derivatives can be explained based on adsorption. In aqueous acidic medium, quinoline derivatives exist in both neutral as well as cationic forms.

$$\text{AHQ neutral} \rightleftharpoons \text{AHQ protonated.} \qquad (4.19)$$

Quinoline derivatives adsorb on the metal surface via displacement of the water molecules adsorbed on the metal surface.

$$M_{H2O} + AHQ \rightleftharpoons M_{AHQ} + H_2O \qquad (4.20)$$

The protonated inhibitor can interact with both the pre-adsorbed Cl^- ions and the cathodic sites. The inhibitor's neutral form can interact with metal by exchanging electrons or sharing the lone pair of electrons. The inhibitor can also interact with the metal surface by absorbing electrons from the metal surface's filled d-orbitals via retro-donation. According to the weight loss data, quinoline derivatives limit corrosion by adsorbing on the metal surface, and the inhibition efficiency improves with inhibitor dosage. The EIS data show an increase in charge transfer resistance, indicating that the inhibitors work by displacing the pre-adsorbed water molecules, causing the cdl values to fall. The mixed character of the inhibitor revealed by the PDP results suggests that it can prevent both anodic (metal disintegration) and cathodic corrosion (hydrogen evolution). The SEM study reveals the creation of a smooth inhibitor layer on the N80 steel substrate, which facilitates inhibitor molecule adsorption. FTIR measurements give additional proof for the inhibitor's adsorption in the acid solution. According to the theoretical characteristics, the AHQ-3 has the lowest energy gap in both the neutral and protonated states. Figure 4.31 depicts a schematic of the adsorption process. The variation in inhibitory efficiency between the three quinoline derivatives can be explained by structural differences. In comparison to AHQ-1, the $-OCH_3$ group is present in the para position of the phenyl ring connected to the quinoline ring in AHQ-2. Because of the electron-donating nature of the $-OCH_3$ group, the inhibitor molecule has a greater inhibitory efficiency. In the case of AHQ-3, the presence of a bond in the inhibitor structure due to the presence of the cinnamaldehyde moiety

promotes conjugation, and the increased geometrical area of the inhibitor molecule gives better metal surface coverage, resulting in enhanced inhibitory efficacy.

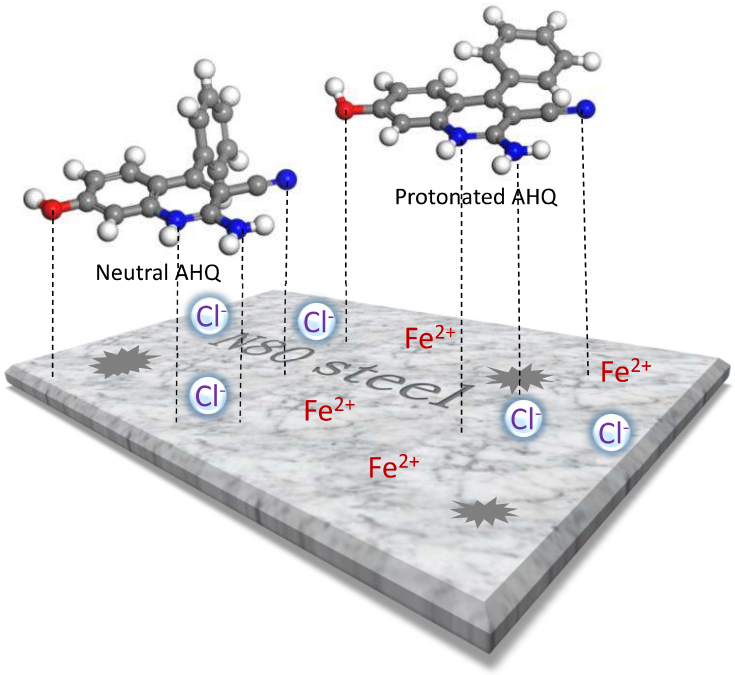

Figure 4.31. Mechanism of adsorption and inhibition

4.3.6 Conclusions.

1. The inhibitory efficiency improved with temperature and reached 97% at a dosage of 300 mg L^{-1}. The inhibition efficiency followed the trend. AHQ-3 > AHQ-2 > AHQ-1.

2. The inhibitor adsorption followed the Langmuir isotherm and had a high G0ads value, indicating chemical adsorption. The inhibition efficacy increased with increasing temperature, suggesting the three inhibitors' robust adsorption.

3. The EIS studies revealed that the inhibitors functioned by adsorbing on the steel surface and that the charge transfer resistance increased with increasing inhibitor concentrations.

4. Polarization measurements revealed that the inhibitors exhibited mixed type adsorption with a cathodic preference and that the inhibitors' adsorption on the metal had no effect on the corrosion mechanism.

5. Surface investigation utilizing SEM measurements revealed that the inhibitors increased the surface smoothness of the steel surface in their presence. FTIR studies revealed the presence of the inhibitors' distinctive functional groups on the metallic surface, as well as the creation of a protective inhibitor coating.

6. The pKa study revealed that the inhibitor molecules have a considerable tendency to protonate at the pyridine nitrogen atom at the observed pH range. The DFT-based quantum chemical parameters corroborated the preceding data and the trend in inhibitory efficiency for AHQ-3 > AHQ-2 > AHQ-1. Monte Carlo simulations found that the protonated AHQ-3 had higher adsorption energy than the neutral molecule, suggesting the inhibitor's principal action in the protonated form.

4.4 (E)-2-styryl-1H-benzo[d]imidazole as novel green corrosion inhibitor for carbon steel.

The acidizing process carried out in the oil and gas sector makes use of steel as the preferred construction material for the oil pipelines [(Dohare *et al*. 2017)]. However, the acids pumped into the pipelines during the stimulation process are highly corrosive, e.g., hydrochloric and sulphuric acids [(Schmitt 1984)]. This causes huge economic losses of the steel structures and can cause potential structural failure. To counter this issue, the use of corrosion inhibitors is one of the most preferred methods. In recent times, there has been a considerable amount of research work undergoing in the area of development of corrosion inhibitors having low toxicity and environmentally benign nature [(Ansari, Quraishi, and Singh 2017)]. In this context, a wide variety of corrosion inhibitors have been reported, e.g., natural extracts, amino acids, carbohydrates, ionic liquids, pharmaceutically active compounds, etc. [(Gece 2011; Verma *et al*. 2018)].

A possible solution could be to explore the environmentally sustainable corrosion inhibitors among the classes of pyridines, pyrimidines, quinolines, azoles, etc. The presence of π-bonds, heteroatoms (N, S, O), phenyl rings introduces multiple adsorption centers in these molecules, which affords improvement in the adsorption [Quraishi *et al.* (2017)]. Among the nitrogen based corrosion inhibitors, the azole family has been one of the widely investigated classes, especially the imidazoles [(Obot and Edouk 2017a),(Aljourani, Raeissi, and Golozar 2009)]. The imidazole is an aromatic molecule that consists of three carbon and two nitrogen atoms having high solubility in the aqueous medium due to its

high polarity. The two N atoms and the aromatic ring provide two effective anchoring sites for coordination with the metal surfaces [Holze *et al*. (1993)]. The introduction of the benzene ring or other functional groups in the imidazole molecule can improve the corrosion inhibition performance of the imidazoles. Several reports are available in the literature describing the corrosion inhibition performance of the imidazole-based corrosion inhibitors for steel surfaces [(Singh *et al*. 2017)].

The benzimidazole is a prominent heteroaromatic bicyclic compound containing a benzene ring adjacent to an imidazole ring. Hoebrecker discovered it, and it is a constituent of Vitamin B12 [(Obot and Edouk 2017b)]. Considering its biological significance, the benzimidazole moiety is considered as environmentally benign (LD_{50} 2910 mg/kg, oral rat). Benzimidazoles exhibit the ability to coordinate metals; therefore, they can effectively mitigate corrosion of metals and alloys. Several reports on the benzimidazole and its derivatives as corrosion inhibitors for a wide variety of corrosive solutions are available in the literature [(Onyeachu, Obot, and Adesina 2020) (Zhang *et al*. 2016)]. Literature review reveals that most commonly, the benzimidazole-based corrosion inhibitors have been utilized in HCl media having concentrations ranging from 0.1 to 1 M [(Marinescu 2019)]. However, the literature shows a scarcity of available reports on the application of benzimidazole derivatives for corrosion inhibition in 15% HCl medium simulating the oil-well acidizing environment.

The prime objective of the present work is to explore a novel corrosion inhibitor 2-styryl-1H-benzo[d]imidazole (STBim) for carbon steel in 15% HCl. The synthesized molecule has

an LD_{50} of 2000 mg/kg, which supports its environmentally benign nature. A unique feature of the present inhibitor is that it can be synthesized from 1,2- diaminobenzene (o-phenylenediamine; PDA) and cinnamaldehyde (LD_{50} 2280mg/kg, oral rat) following the famous Weidenhagen method [(Marinescu 2019)]. The beauty of this method is that this procedure takes place at room temperature within 15–20 min. This is contrary to the other heterocyclic molecules-based corrosion inhibitors, which require a tedious synthetic procedure, sophisticated instrumentation, are considerably costly and toxic.

In addition, a number of green chemistry metrics were evaluated for the STBim molecule to analyze the environmentally benign nature of the inhibitor. The presence of π-bond and the phenyl ring of the cinnamaldehyde moiety, together with the benzimidazole framework, is likely to impart significant adsorption and inhibition capabilities to the studied molecule. The synthesized molecule has a considerably large molecular structure, which can provide efficient coverage of the metal surface. A detailed study on the gravimetric, electrochemical, and surface analytical measurements is presented in this investigation. The experimental studies were fortified by the assessment of inhibitor adsorption via a detailed DFT-based computational simulation.

4.4.1 Weight loss measurements.

4.4.1.1 *Influence of STBim concentration.*

The gravimetric test gives the simplest yet the most reliable measurement of the corrosion inhibition performance of inhibitors. Therefore, it is a general practice to perform this analysis prior to undertaking more sophisticated studies.

The influence of inhibitor dosage on the variation in the inhibition efficiency was studied by introducing the varying dosages of the STBim ranging from 5 to 200 $mgL^{-1.}$ The results on the influence of the effect of concentration are shown graphically in Figure 4.32(a). It is obvious from the curve that the addition of the increasing inhibitor concentrations caused the corrosion inhibition to rise successively, and it attained >98% efficiency at 200 mgL^{-1}. The high efficiency of the STBim molecule can be ascribed to the π-bond and the additional phenyl ring of the cinnamaldehyde moiety, which can provide efficient coverage of the carbon steel. The inhibitor molecules, when added in the increased amounts, can adsorb at the steel substrate and cover the corrosion active sites.

4.4.1.2 Influence of temperature.

The oil-well acidizing process requires the use of high temperatures. The elevated temperatures can cause inhibitor desorption from the metallic surface. For a corrosion inhibitor to be considered as potentially applicable in the oil and gas sectors, it is important to evaluate the corrosion inhibition behavior at the higher temperatures. Therefore, in the present study, the influence of temperature was studied via gravimetric measurement in the range of 303 K to 333 K. The results of the variation in the inhibition efficiency versus the solution temperature are displayed in Figure. 4.32(b). A notable observation that the inhibition efficiency remained almost constant and showed a negligible decline with the rise in the temperature. This kind of behavior is attributed to a strong interaction between the inhibitor molecule and the metal surface.

The rise in the temperature of the solution also produced an increase in the corrosion rate (CR) of the blank as well as the inhibited samples. The Arrhenius equation is commonly used to elucidate the relationship between the temperature and the corrosion rate (CR) [(Chauhan *et al*. 2019)]:

$$C_R = A\exp(\frac{-Ea}{RT}) \qquad (4.21)$$

where A denotes the Arrhenius pre-exponential factor, Ea is the energy of activation and other symbols have the usual denotations. The Arrhenius plots for the steel surface without and in the presence of the STBim inhibitor are given in Figure. 4.32(c). The slope of these curves equals to Ea/2.303R, which can be used for the calculation of the Ea values. The Ea for the blank carbon steel and in the presence of the STBim inhibitor are 32.95 kJ mol^{-1} and 65.05 kJ mol^{-1}. The higher value of the Ea in the presence of the inhibitor compared to that in the blank sample indicates an increase in the energy barrier required to be crossed for the corrosion and dissolution process. This supports that the inhibitor STBim adsorbed on the steel sample and formed a protective film, which minimized the corrosive dissolution of the metallic substrate.

4.4.1.3 Adsorption considerations.

The adsorption of an inhibitor molecule on the surface of a metallic substrate can be elucidated with the help of a suitable adsorption isotherm [(El-Hajjaji *et al*. 2018)]. Critical parameters influencing the adsorption of an organic compound include the structure of the inhibitor molecule, solution temperature, nature of the metallic adsorbent, etc. The adsorption of the corrosion inhibitor molecule STBim was studied by fitting the

experimentally obtained data to a number of isotherms viz. Temkin, Frumkin, Freundlich, and Langmuir [(Chauhan *et al.* 2019)]. Among the tested isotherms, the Langmuir isotherm showed the most suitable fit. According to the Langmuir adsorption isotherm, the film of the inhibitor molecules formed on the metal surface has a thickness of the order of a monolayer [(Abdallah 2002)]. Also, the isotherm considers that all the equilibrium adsorption sites are similar and are having an equal affinity for the adsorbate molecule, and there is no interaction taking place between the adsorbed molecules. Therefore, this isotherm indicates the occurrence of homogeneous adsorption. The isotherm can be given in equation 4.1:

Herein, the symbols K_{ads} and C denote the equilibrium constant for the adsorption, and C is the concentration. The Langmuir plot of the inhibitor adsorption in 15%HCl is given in Figure 4.32(d). The slope and the regression coefficient are close to 1, which validates the successful fitting of the Langmuir isotherm [(Abd El-Lateef and Alnajjar 2020)]. Using the Kads values, the standard free energy of adsorption (ΔG^0_{ads}) was computed using the equation given in equation 3.14.

where the term 1 × 106 represents the concentration of water in gL^{-1}, and the other symbols have their usual meanings. The adsorption of a corrosion inhibitor on a metallic substrate involves both the physical and the chemical adsorptions. The calculated ΔG^0_{ads} value was −45.774 kJ g^{-1}, suggesting that in the present investigation, the STBim inhibitor undergoes chemical adsorption on the surface of metal [(Abd El-Lateef and Alnajjar 2020]. This negative sign shows the spontaneity of the inhibitor adsorption.

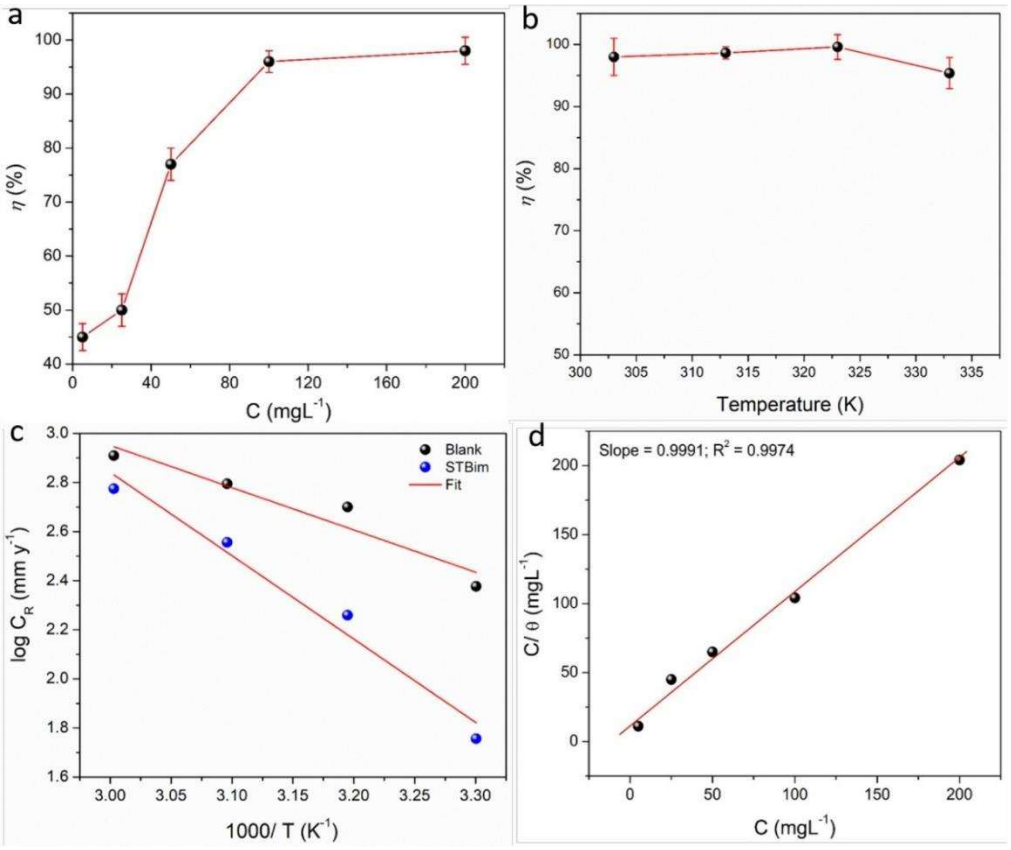

Figure 4.32 (a) Variation of inhibition efficiency with concentration of STBim obtained from the weight loss measurements; **(b)** Variation of the inhibition efficiency with temperature; **(c)** Arrhenius plots for steel surface without and with inhibitor; **(d)** Langmuir isotherm plot for the adsorption of STBim on the steel surface.

4.4.2 Electrochemical investigations.

4.4.2.1 Impedance analyses.

The open circuit potential (OCP) describes the working electrode potential with reference to that of the reference electrode under the condition of the absence of any applied potential

or current. The OCP measurements are run before conducting the EIS, and the PDP studies in the electrochemical corrosion evaluation of inhibitor molecules [(Yadav, Quraishi, and Maiti 2012)]. Figure 4.33 shows the variation in the OCP vs. time plots of the carbon steel substrate immersed in the 15% HCl solution without and containing the varying concentrations of the corrosion inhibitor STBim. With increasing inhibitor concentration, the OCP curves shift towards the greater negative directions suggesting the formation of a protective inhibitor film on the metallic substrate [(Chauhan *et al*. 2019)].

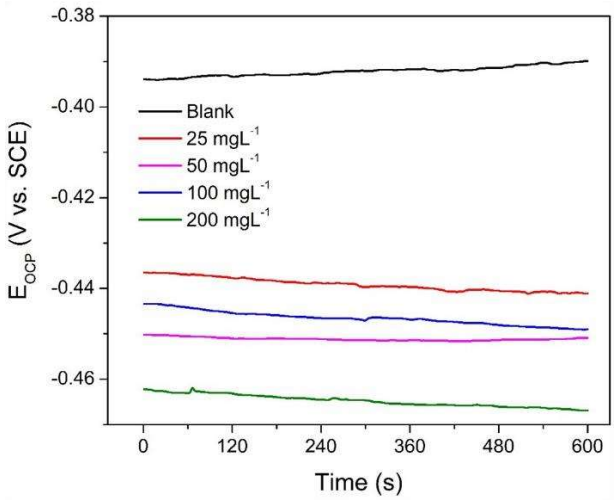

Figure 4.33 Open circuit potential vs. time curves for carbon steel surface in 15% HCl without and with varying concentrations of STBim.

The impedance measurements present a convenient and nondestructive means to analyze the interfaces of solid metallic substrates immersed in an electrolytic solution [(Onyeachu, Obot, and Adesina 2020; Sudheer and Quraishi 2013; Solmaz 2010)]. The corrosion inhibition behavior of the STBim molecule was studied using the EIS analysis, and the

obtained results are graphically shown in the form of the Nyquist plots in Figure 4.34 (a) [(Abdrabo *et al.* 2020)]. Both in the absence of the inhibitor (blank carbon steel) and the varying dosage of the STBim inhibitor, single depressed semicircles were observed having their center below the real x-axis. This type of behavior is typical of the metallic electrodes undergoing corrosive attack of the acidic electrolytes [(Chauhan *et al*. 2019) (Ansari *et al.* 2020*;* Baig *et al*. 2019)]. The electrochemical data were modeled using the equivalent circuit provided in Figure 4.34 (e) and Figure 4.34(f) for the uninhibited and with STBim samples. The equivalent circuit diagram resembles the modified Randle's circuit, which contains the Rs (solution resistance), the R_{ct} (charge transfer resistance), and a constant phase element (CPE) in place of the classical double layer capacitor. For the inhibited samples, another resistance/capacitance (RC) combination can be visualized, containing the contribution from the film in the form of the CPE_f and its corresponding film resistance (R_f). The CPE impedance can be given in equation 3.5:

where Y_0 denotes a coefficient of proportionality, ω is the angular frequency, n is CPE exponent with values between 0 and 1, and provides a gauge for the surface heterogeneity. With a rise in the concentrations of the STBim inhibitor, there is a continuous rise in the Nyquist diameter. This suggests that the inhibitor is adsorbing, and it forms a protective film, which retards the processes of charge and the mass transfer phenomena. The inhibition efficiency was calculated as [(Chauhan *et al*. 2019)]:

$$\eta_{EIS}(\%) = \frac{R^{inh}{}_P - R_P}{R_P} \qquad (4.22)$$

where, R_p and R^{inh}_p denote the polarization resistances without and containing the inhibitor, respectively. Wherein, the Rp is equal to the R_s+R_{ct} for the blank steel sample as described previously [(Wang, Yang, and Wang 2011; Haque *et al*. 2018)]. In the case of the inhibited samples, the Rp is the collective contribution of the resistance from the R_s, R_{ct} and R_f [(Wang, Yang, and Wang 2011; Haque *et al*. 2018)]. The increase in CPE value upon the addition of the first concentration of the inhibitor may be attributed to the permeation of aggressive species through the porous film, which can initiate the corrosion at the inhibitor/ metal interface. This type of behavior has been reported by many researchers [(Hang *et al*. 2012; Cao *et al*. 2019)]. The subsequent lowering in the CPE values can be ascribed to the improvement in the capacitive performance due to the adsorption of the inhibitor at the metal/ solution interface [Cao *et al*. 2019) (Fernandes *et al*. 2019)]. The Bode and the phase angle curves for the uninhibited steel samples and the samples with inhibitor are displayed in Figure 4.34 (b). The curves obtained for the inhibited samples confirm the appearance of a two time-constant processe. The deviation from the ideal capacitive performance (slope −1 and phase angle −90°) can be attributed to the heterogeneity of surface resulting due to the corrosion process of the carbon steel surface [(Singh *et al*. 2017)]. However, in the inhibited samples, the approach of the slope and the phase angle towards the ideal values can be attributed to the corrosion inhibition behavior of the STBim inhibitor [(Onyeachu, Obot, and Adesina 2020; Popova and Christov 2006)]. The organic inhibitor molecules adsorb at the metal/ solution interface by replacing the preadsorbed water molecules. This causes a lowering of the local dielectric constant and also a

thickening of the double layer. Together these two factors cause an improvement in the capacitive behavior along with an increase in the inhibition efficiency. The electrochemical data were fitted to the equivalent circuit diagram to obtain the electrochemical parameters, which are listed in Table 4.12 with the inhibition efficiency. The fitted Nyquist plots in the absence and with the STBim inhibitor are displayed in Figure 4.34(c), and the corresponding fitted Bode, phase angle plots are shown in Figure 4.34(d). The goodness of fit parameter ($\chi 2$) shows considerably low values, suggesting the accuracy of the fitted EIS data.

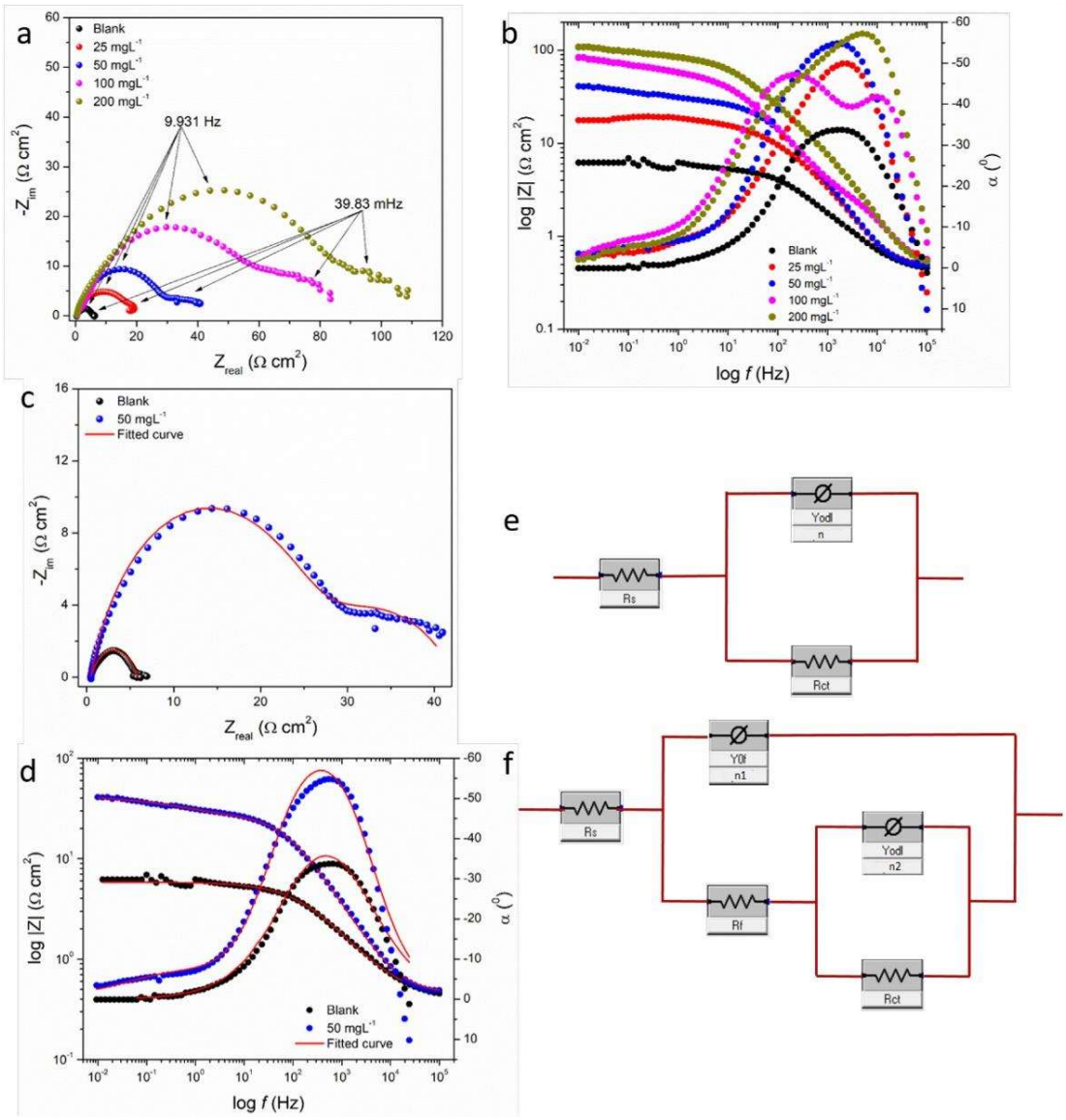

Figure 4.34 (a) Nyquist; **(b)** Bode, and phase angle plots for the adsorption of STBim on the carbon steel surface in 15% HCl. Fitted **(c)** Nyquist; **(d)** Bode, phase angle plots obtained for carbon steel in the absence and the presence of STBim in 15% HCl. Equivalent circuit models used to fit the EIS data obtained for the **(e)** blank and **(f)** inhibited steel samples.

Table 4.12 Electrochemical impedance parameters for carbon steel sample in 15% HCl at different concentrations of STBim

Inhibitor (mgL^{-1})	R_s (Ω)	CPE_f ($Y_0 \times 10^{-6}$ ($\mu F/cm^2$)	n1	R_f (Ω cm^2)	CPE_{dl} ($Y_0 \times 10^{-3}$ ($\mu F/cm^2$)	n2	R_{ct} (Ω cm^2)	$\chi^2 \times 10^{-3}$	ηEIS (%)
Blank	0.415	–			3.087	0.65	6.87	2.991	–
25	0.520	535.5	0.66	1.50	4.361	0.63	15.55	2.714	61.83
50	0.451	411.2	0.68	14.58	3.541	0.68	29.48	6.255	84.02
100	0.440	309.1	0.73	23.57	2.310	0.66	58.34	1.628	91.51
200	0.457	125.2	0.74	27.44	1.219	0.63	83.31	1.415	93.75

4.4.2.2 Frequency modulations.

The EFM measurements allow the analysis of the electrical interfaces and can provide the anodic and the cathodic Tafel slopes without the need to run the polarization experiment [(Obot and Edouk 2017b, 2)]. A unique feature of the EFM technique is the causality factor 2 and causality factor 3 that provide internal validation of the EFM results. In the present case, the EFM technique was undertaken without and with the STBim inhibitor in varying doses, and the results in the form of the EFM curves are given in Figure 4.35. The different EFM parameters can be explained as follows [(Onyeachu, Obot, and Adesina 2020)]:

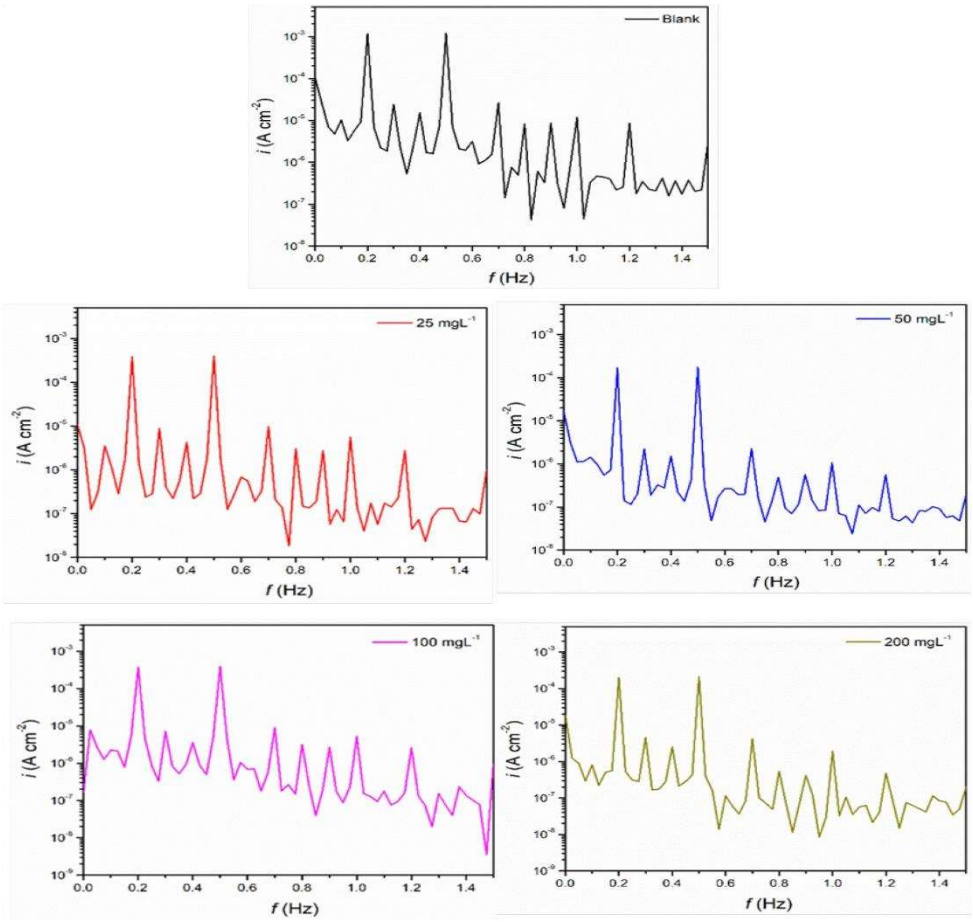

Fig. 4.35. Intermodulation spectra obtained from the EFM measurements for the carbon steel immersed in 15% HCl solution in the absence and the presence of different concentrations of STBim.

$$i_{corr} = \frac{i^2_{\omega}}{\sqrt{48(2i_{\omega}i_{3\omega} - i^2_{2\omega})}} \tag{4.23}$$

$$\beta a = \frac{i_{\omega}U_0}{2i_{2\omega} + 2\sqrt{3}\sqrt{2i_{\omega}i_{3\omega} - \iota^2_{2\omega}}} \tag{4.24}$$

$$\beta c = \frac{i_\omega U_0}{2\sqrt{3}\sqrt{2i_\omega i_{3\omega} - i^2_{2\omega} - 2i_{2\omega}}} \quad (4.25)$$

$$\text{Casuality factor (2)} = \frac{i_{\omega 2 \pm \omega 1}}{i_{2\omega_1}} = 2.0 \quad (4.26)$$

$$\text{Casuality factor (2)} = \frac{i_{\omega 2 \pm \omega 1}}{i_{3\omega_1}} = 3.0 \quad (4.27)$$

The calculated EFM parameters are displayed in the Table 4.13. The corrosion currents show a lowering with the STBim dosage, and the inhibition efficiencies show a corresponding increase with increasing inhibitor dose. The causality factors 2 and 3 are approaching towards their established values of 2 and 3, respectively, which verifies the accuracy of the obtained EFM data.

Table.4.13 Electrochemical EFM parameters obtained for carbon steel sample in 15% HCl without and with different concentrations of STBim.

Inhibitor (mgL^{-1})	i_{corr} (μAcm^{-2})	CF 2	CF 3	ηEFM%
Blank	1587 ± 42	2.13	3.13	-
25	728 ± 39	2.05	3.13	54.12 ± 0.5
50	409 ± 28	2.06	3.05	74.22 ± 0.7
100	184 ± 15	2.13	3.12	88.40 ± 0.9
200	92 ± 7	1.93	2.99	94.20 ± 0.9

4.4.2.3 Polarization studies.

The knowledge of the electrochemical kinetics of the adsorption and the inhibition behavior of a corrosion inhibitor can be obtained via PDP measurements [(Tang *et al.* 2013; McCafferty 2005; Abd El-Lateef and Alnajjar 2020)]. In the present study, the PDP experiments were carried out in the blank and with the varying inhibitor concentrations, and the results are displayed as the Tafel plots in Figure 4.36. From the extrapolation of the linear segments of the Tafel curves, the electrochemical parameters were obtained and are given in Table 4.13. The corrosion inhibition efficiency was calculated using the corrosion current densities (i_{corr}), as shown in equation 3.9:

i_{corr0} and i_{corri} show the corrosion current densities in the blank and with the inhibitor STBim. Table 4.14 depicts that the inhibition efficiency reaches a high value of 93.75% at 200 mgL^{-1}. Another observation, which can be made from the Tafel plots, is that the anodic and the cathodic current curves show a lowering. This suggests that the addition of the STBimto the corrosive solution produces an inhibitor film, which lowers both the anodic metal dissolution and the cathodic hydrogen evolution. Further, an obvious shift can be observed in the corrosion potentials (E_{corr}), towards the cathodic directions. This suggests that the inhibitor displays a mixed nature with the cathodic prevalence.

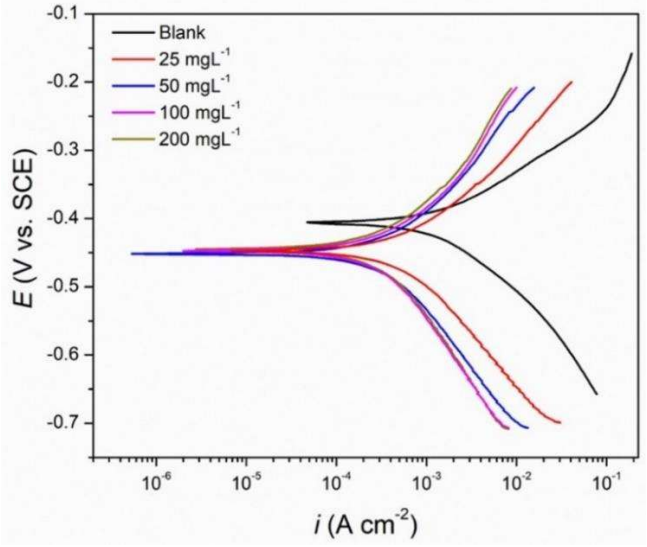

Figure 4.36 Potentiodynamic polarization curves obtained for the carbon steel immersed in 15% HCl solution in the absence and presence of different concentrations of STBim.

Table 4.14 Potentiodynamic polarization parameters for carbon steel in 15% HCl obtained at different concentrations of STBim.

Inhibitor (mgL^{-1})	i_{corr} (μAcm^{-2})	$-E_{corr}$ (mV/SCE)	βa (mV/dec)	-βc (mV/dec)	$\eta_{PDP\%}$
Blank	1649 ± 39	393	67.1	141.1	
25	749 ± 33	448	79.1	154.3	54.75 ± 0.5
50	358 ± 32	442	68.4	152.4	78.28 ± 0.8
100	217 ± 22	445	75.3	158.3	86.84 ± 0.8
200	103 ± 9	451	81.3	163.6	93.75 ± 0.9

4.4.3 Surface studies.

4.4.3.1 Atomic force microscopy.

The surface analysis of the inhibitor-adsorbed steel surface was performed to understand the influence of inhibitor adsorption on the surface morphology of the carbon steel. The corresponding AFM images are shown in Figure 4.37 (a, b) in the absence and presence of the inhibitor STBim (in optimum concentration). The blank steel surface shows a considerable amount of surface damage in the form of a number of peaks and striations, which can be accounted to the corrosive damage.

However, with the inhibitor, a considerably smooth surface image of the metallic substrate is observed. The roughness of the surface in the blank sample was 260 nm, which decreased to 46 nm with the STBim. This shows that the addition of the inhibitor to the corrosive electrolyte leads to the inhibitor adsorption on the metallic substrate and the formation of a smooth film, which significantly improved the surface smoothness of the metallic substrate.

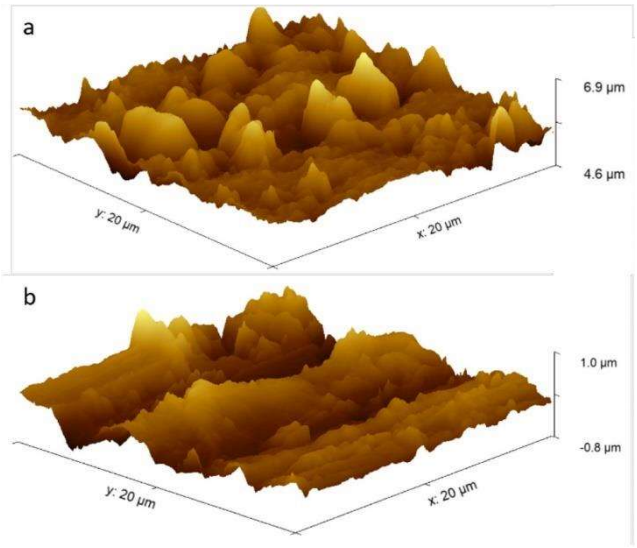

Figure 4.37 Fe-slab and (E)-2-styryl-1H-benzo[d]imidazole (STBim)models used in our DFT simulation. **a)** An overview of the Fe-slab and the adsorbate with 25 Å vacuum to ensure that there is no interaction between the slab and its image along C-lattice constant. **b)** The optimized structures of STBim+ on Fe-slab, Color code, C: brown, N: blue, and H: white.

4.4.3.2 FTIR studies.

The FTIR measurements can provide direct evidence of the adsorption of inhibitor adsorption on a metallic surface in a given corrosive medium. The FTIR-ATR images of the pure STBimand that of the carbon steel surface following immersion in the 15% HCl in the presence of the inhibitor STBim are shown in Figure 4.38 (c,d). The characteristic peaks of the inhibitor STBimare as follows (ν; cm^{-1}): 3376 (N–H stretch), 1590 (inplane N–H), 1365 (ring C–N), and 1259 (in-plane C–N). The spectrum of the carbon steel sample after immersion in the presence of the STBim inhibitor shows a broad

band around 3500 cm^{-1} occurring due to the collective contribution of the N–H stretch as well as due to the –OH stretch of the adsorbed water molecules. The in-plane N–H stretch now appears at 1633 cm^{-1}. Other peaks are not clearly visible, which is expected due to the presence of the trace amount of the inhibitor on the metallic substrate after immersion [(Chauhan *et al.* 2019)]. The spectrum of the inhibited sample retains the significant peaks of the pure STBim inhibitor, supporting the inhibitor adsorption on the steel surface.

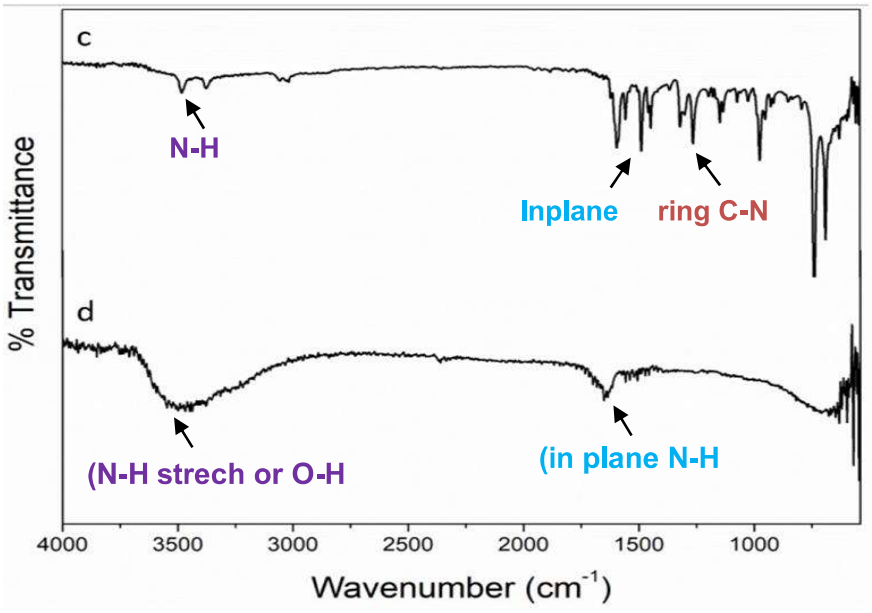

Figure 4.38 FTIR spectra of the **(c)** pure STBim **(d)** STBim adsorbed carbon steel surface after immersion in 15% HCl.

4.4.4 Theoratical studies.

4.4.4.1 DFT simulations.

Two protonated forms of STBim (STBim+, and STBim) were used for the adsorption on Fe-slab (100) simulation (see Figure. 4.39). We also have considered two configurations of

STBim on Fe-slab (STBim-I, and STBim-II, Figures.4.39 (c) and (d)) to study the conformational preference of STBim adsorption on the Fe-slab. The two conformations of STBim considered in our study are; STBim-I in which the molecular plane of the neutral STBim is parallel to themetal surface while it is perpendicular to the metal surface in STBim-II conformation.

Periodic Density Functional Theory (DFT) simulations are employed in order to examine the adsorption of STBim molecule on Fe-slab (100) [(Kokalj 2013; Guo et al. 2018)]. First, we have optimized two protonation states and two configurations of the neutral form on Fe-slab, as depicted in Figure. 4.39. The Adsorption energies of $STBim^{+}$, STBim-I, and STBim-II are −10.61, −8.78, and −1.54 eV, respectively. These adsorption energies indicate a favorable binding between Fe-slab and STBim, whatever its protonation form or its orientation on the slab. However, the adsorption of the protonated formis significantly dominant. As expected, the parallel adsorption of the neutral form of STBim-I is more favorable than the axial one as in this orientation, STBim-I maximizes its interaction with the slab; therefore, we focus only on the following on the parallel one. The charge density binding analysis [(Tozini et al. 2015)]. Depicted in Figure. 4.40. put in evidence the chemisorption nature of STBim as there is an accumulation of the electronic density between Fe–C bond. The interaction of Fe slab with STBim molecule has the pattern Fe–C=C interaction. Fe–C bond distances range from 1.98 Å to a maximum of 2.50 Å, with most of the bonds have a distance of around 2.0 Å, which support a covalent interaction between Fe-slab and STBim molecule (see Fig. 4.41 and Table 4.15). The strength of the

adsorption does not originate only from a covalent interaction between Fe and C atoms but also from the strong electrostatic interactions at their interface.

In order to gain deeper insights into the electronic flow along Fe slab@ molecule interface, we have calculated the atomic charges using the AIM approach using Bader code as detailed in the methods section.

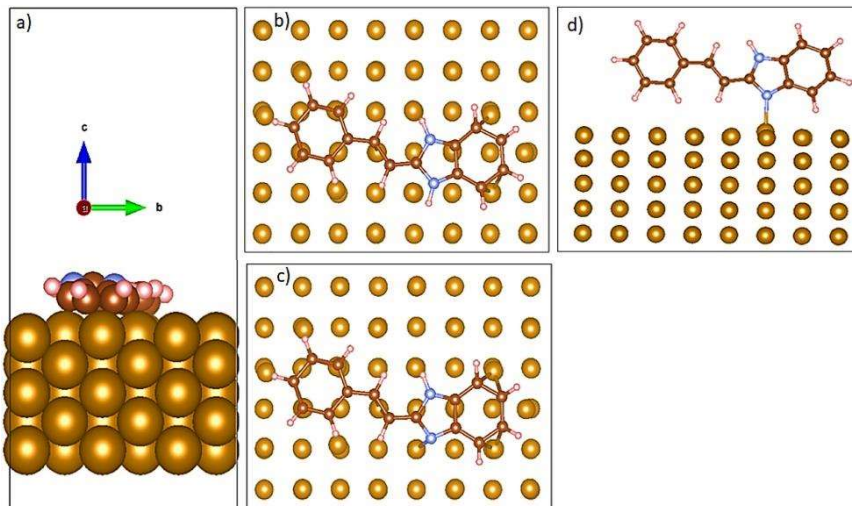

Figure. **4.39** Fe-slab and (E)-2-styryl-1H-benzo[d]imidazole (STBim) models used in our DFT simulation. **a)** An overview of the Fe-slab and the adsorbate with 25 Å vacuum to ensure that there is no interaction between the slab and its image along C-lattice constant. **b)** The optimized structures of $STBim^{+}$ on Fe-slab, **c)** Fe-slab + STBim-I, and **d)** Fe-$slab^{+}$ STBim-II complexes. Color code, C: brown, N: blue, and H: white

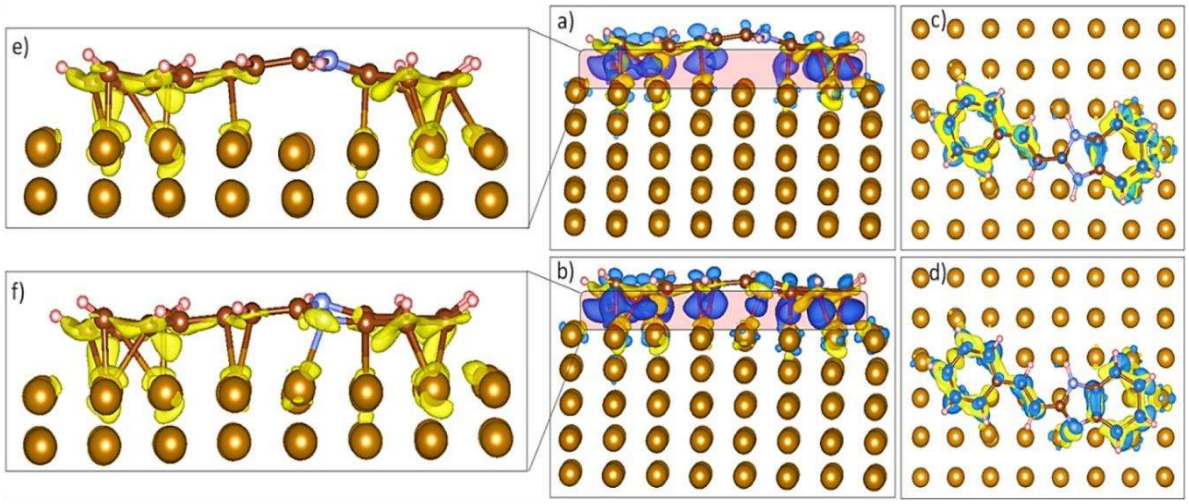

Figure. 4.40. The binding charge densities of STBim+, and STBim on Fe-slab (100) analysis are shown, they are calculated following Eq. (3), we have subtracted the electron densities of the isolated slab and molecule from the total electron density of the complex. This analysis showing the interaction sites between the molecule and the slab. **a**), and **c**) the binding density of $STBim^+$ side and top view. **b**), and **d**) is the binding charge density of STBim on Fe-slab, side and top view. **e**), and **f**) are zoom in images of $STBim^+$ and STBim on Fe-slab showing only the accumulation of the electronic density (yellow), respectively. The isosurfaces is represented in a resolution of 0.005 electron/Å3. Yellow is rich and light-blue is depletion of the electron density. Fe-slab is represented by brown spheres, STBim is represented in balls and sticks. Color code, C: brown, N: blue, and H: white.

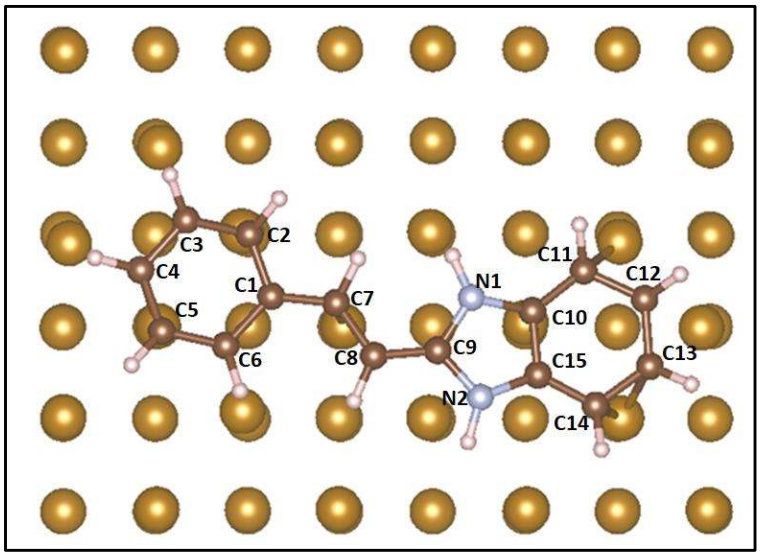

Figure. 4.41: The protonated $STBim^{+}$ adsorbed on the iron slab with numbering of the heavy atoms to show the Fe-C bond distances reported in Table 4.15

Table 4.15: The optimized Fe-C bond distances between the adsorbate and slab for $STBim^+$ and STBim-I. Carbon and Nitrogen numbering is following scheme shown in Figure 4.41.

Bond	Fe_2-PBIM$^+$	Fe_2-PBIM-I
Fe-C1	2.51	2.36
Fe-C2	2.03	2.01
Fe-C3	2.17	2.20
Fe-C4	2.17	1.98
Fe-C5	2.01	2.21
Fe-C6	2.36	2.24
Fe-C7	2.13	2.12
Fe-C8	2.42	2.19
Fe-C9	3.0	2.68
Fe-C10	2.19	2.16
Fe-C11	2.10	2.12
Fe-C12	2.28	2.23
Fe-C13	2.07	2.01
Fe-C14	2.13	2.19
Fe-C15	2.55	2.22
Fe-N1	2.85	2.96
Fe-N2	2.88	2.09

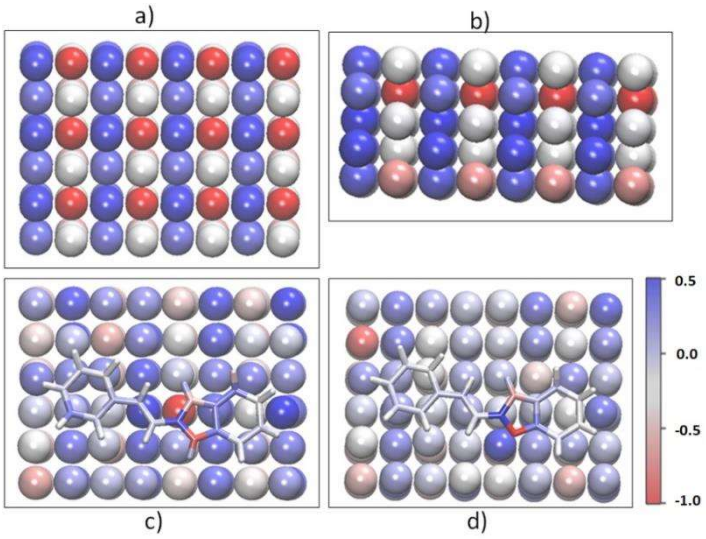

Figure 4.42: show iron Fe-slab and adsorbed inhibitors colored by the atomic charges calculated using AIM approach, a color scale from 0.5 to -1.0e is shown. A clean iron slab is shown in two different views **a**): top view, and **b**) side view. **c**) and **d**) show the adsorbed $STBim^{+}$, and STBim-I on Fe-slab, respectively. Adsorbate are shown in sticks and metal surface are shown spheres

The calculation of atomic charges (see Figure. 4.42 and Table 4.16) show clearly a strong charge transfer. First, the covalent interaction between Fe and C-C bonds of STBim resulted from hybridization of π-orbital of the adsorbate and d-orbital of Fe atoms and so electronic donation from the adsorbate to the vacant d-orbital of Fe atoms. This electronic transfer is accompanied by a back-donation from the occupied d-orbitals of Fe atoms into the empty π*-orbital of the adsorbate [(Koch et al. 2019), (Cramer and Truhlar 2009)]. Indeed, the total charge of the adsorbate in all the considered conformations is negative,

which highlights that the back-donation is dominated the total electronic flow at the metal@adsorbate interface. Actually, in the case of Fe-slab@STBim$^+$ complex, Fe-slab has total charge of 3+, this indicates that there is 3.0e transferred from the metal surface to the adsorbate. Similarly, in the case of the neutral form, there is 2.37e transferred from the metal surface to the adsorbate. As we can observe, the adsorption strength is correlated well with the amount of charge transfer from the metal surface to the adsorbate, which boosts up the electrostatic interaction between the molecule and the slab.

The atomic charges reported in Table 4.16 and visualized on the molecularmodels depicted in Figure. 4.42 put in evidence the effect of STBim adsorption on the polarity of the iron slab. In a clean Fe-slab, the surface is highly polarized with the accumulation of the negative charges close to the surface. However, upon the adsorption, this polarization is almost disappeared and localized at the interface between the metal surface and STBimmolecule. It is important to mention that there is no tight interaction between the nitrogen atoms and Fe atoms due to the electrostatic repulsion between the lone pair electrons on nitrogen atom and the d-orbital electrons of Fe atoms. Upon the protonation of the second nitrogen atom, this electrostatic repulsion is diminishing, which allows more electron transfer fromthemetal surface to the vacant π^*-orbital of STBim$^+$ molecule.

As a final remark, the binding charge density reveals an important point: the origin of the chemisorption of the STBim molecule is due to the interaction of the isolated phenyl and the phenyl of the benzimidazole moiety as well as the linker ethylene with Fe atoms.

We have further calculated the work function of the clean surface and the complex with the neutral and the protonated STBim molecule to link with its corrosion efficiency. The planar average of the electrostatic potential along Z-axis for the three forms of STBim molecule adsorbed on Fe-slab, and the clean slab is shown in Figure. 4.43. The work function (φ) is defined as the minimum energy required to extract an electron from the metal surface or the energy required to move an electron from the Fermi level into a vacuum.

The binding charge densities of $STBim^{+}$, and STBim on Fe-slab (100) analysis are shown, they are calculated following Eq. (3), we have subtracted the electron densities of the isolated slab and molecule from the total electron density of the complex. This analysis showing the interaction sites between the molecule and the slab. a), and c) the binding density of $STBim^{+}$ side and top view. b), and d) is the binding charge density of STBim on Fe-slab, side and top view. e), and f) are zoom in images of $STBim^{+}$ and STBim on Fe-slab showing only the accumulation of the electronic density (yellow), respectively. The isosurfaces is represented in a resolution of 0.005 electron/Å3. Yellow is rich and light-blue is depletion of the electron density. Fe-slab is represented by brown spheres, STBim is represented in balls and sticks. Color code, C: brown, N: blue, and H: white.

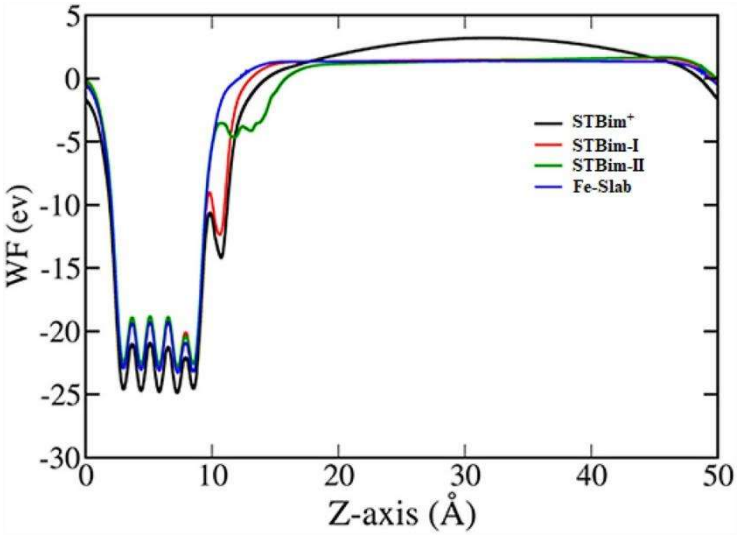

Figure. 4.43. The planar average of the electrostatic potential along Z-axis for the three form of STBim molecule adsorbed on Fe-slab and the clean slab.

$$\Phi = V_{vac} - E_f \qquad (4.28)$$

where V_{vac} is the electrostatic potential in the vacuum region, and Ef is the Fermi level. The work function was calculated using 50 Å as a vacuum to ensure the convergence of our results with the vacuum depth. It was found to be 7.28 eV for STBim+, 3.70 eV for STBim-I, 3.66 eV for STBim-II, and 3.82 eV for the clean iron slab (Exp. is 4.67 eV) . It is obvious that the inhibition efficiency of the STBim molecule originates fromthe protonated form,which has the highest work function. In contrast, the work function of the neutral form does not change significantly from the clean Fe-slab. It is also worth to mention that PBE functional is underestimating the work function of the metal surfaces, and it depends on the number of slab's layers that increases the cost of the calculations; however, we

herein are interested in the relative trend of the work function rather than the absolute values.

Altogether, DFT simulations predicted that the adsorption of STBim is chemical rather than physical. An accumulation of the electron density at the interface Fe-slab: molecule interface along with Fe–C=C bond evidence the chemisorption of the molecule. The adsorption of the protonated form is significantly dominated. Further, the electron transfer from themetal surface to the adsorbate boosted up the electrostatic interaction between the slab and adsorbate, which enhances its stability. The main group of the interaction of the STBim with Fe surface is the phenyl groups and the C- C linker, as demonstrated by the charge density difference. The protonated form resulted in a substantial increase in the Fe-slab work function, which is the origin of its corrosion inhibition efficiency.

4.4.5 Mechanism of corrosion inhibition.

Weight loss investigations, electrochemical measurements, surface analysis, and computational methods were used to examine the adsorption and corrosion inhibition behaviour of the STBim molecule for carbon steel in 15% HCl. The increase in inhibition efficiency with increasing inhibitor concentration, as measured during gravimetric tests, indicates that the inhibitor works by adsorption on the metal surface. The EIS, EFM, and PDP tests revealed a rise in polarisation resistance and a decrease in corrosion current densities, which confirmed inhibitor adsorption on the metal surface [(Chauhan et al. 2020)]. The inhibitor adsorption on the steel surface caused a shift in the corrosion potential, supporting the cathodic predominance of the inhibitor action. An organic

corrosion inhibitor molecule can exist in the protonated form in aqueous corrosive solution, as indicated by the equilibrium below:

$$STBim_{neutral} \rightleftarrows STBim_{protonated} \quad (4.29)$$

The inhibitor can undergo adsorption on the steel surface via replacement of the pre-adsorbed water molecules, as shown below:

$$MH_2O + STBim \rightleftarrows MSTBim + H_2O \quad (4.30)$$

The PDP investigation demonstrated a mixed type of inhibitor effect with a reduction in both anodic and cathodic currents, indicating that the inhibitor has a proclivity to adsorb on both anodic and cathodic corrosion active sites present on the metal surface. Through electrostatic contact, the protonated version of the inhibitor molecule can directly adsorb on the cathodic corrosion active sites present on the metal surface [(Yadav, Quraishi, and Maiti 2012)].

The pre-adsorbed Cl ions on the positively charged steel surface form a bridge type of interaction with the protonated inhibitor molecules on the anodic sites, aiding adsorption. Furthermore, the electrons can be returned to the inhibitor molecule via the metal surface's filled d-orbitals.

Surface smoothness studies using AFM revealed a quantitative improvement in the presence of the corrosion inhibitor, which validated the adsorption and inhibition performance. The presence of the adsorbed inhibitor on the metal surface was also

confirmed by FTIR studies. The presence of the inhibitor in the protonated form was discovered by pKa analysis in theoretical studies. The DFT calculations shed more light on the inhibitory mechanism. It was discovered that the neutral version of the corrosion inhibitor had poorer adsorption on the steel surface. In contrast, the protonated version of the inhibitor displayed more adsorption on the metal surface. This corroborated the mixed mode of corrosion inhibition reported by the PDP investigations.

4.4.6 Conclusions.

The current study describes a benzimidazole-cinnamaldehyde derivative, called the STBim molecule, as a new inhibitor for carbon steel in 15% HCl based on extensive experimental and computational analyses. The compound has a high LD_{50} value of 2000 mg/kg and was created using a straightforward chemical technique. A number of green chemistry indicators were tested, revealing the molecule's ecologically benign characteristics.The current investigation leads to the following major conclusions:

1. Gravimetric measurements exhibited an increase in corrosion inhibition efficacy with increasing inhibitor concentration, reaching >98% at a dosage of 200 mgL^{-1} and demonstrating robust adsorption by retaining an efficiency of >95% even at 333 K. The Langmuir isotherm was followed by inhibitor adsorption on carbon steel, and the ΔG^{o}_{ads} value indicated both physical and chemical adsorption.

2. The EIS study demonstrated the existence of a two-time constant phenomenon for inhibitor adsorption. EFM measurements revealed that inhibitor adsorption on the steel

substrate reduced corrosion currents, which was verified by the theoretical values of the causation factors.

3. The PDP analysis revealed that inhibitor adsorption resulted in a mixed type behaviour with cathodic preponderance.

4. AFM tests revealed a smoother surface topography as compared to the blank sample, as well as a quantitative improvement in the smoothness of the steel surface. The FTIR tests supported the corrosion inhibitor's adsorption on the metallic substrate.

5. DFT calculations revealed that the neutral inhibitor form exhibited weaker adsorption due to repulsion between the lone pair electrons of the imidazole ring's N atom and the filled d-orbitals of the Fe atoms. This repulsion diminished in the protonated form, and the inhibitor adhered more strongly on the Fe surface. The work function of the neutral inhibitor/Fe-slab was found to be substantially lower than that of the protonated inhibitor/Fe-slab, indicating that the inhibitor adsorbs more readily in the protonated form than in the neutral form. The work function calculations revealed that the source of STBim inhibition is due to the stability of the metal surface valence band, which resulted in a 3.46 eV change of the metal surface work function.

6. The present study could be enhanced by investigating the influence of different substituent groups on inhibitory efficiency, which could be backed by theoretical studies. Another possibility is to use halide ions as synergistic agents to boost inhibition efficiency at lower inhibitor concentrations. The presence of the protonated version of the inhibitor suggests that more research into synergistic corrosion inhibition is warranted.